



Regional stress and predicted hydrogeochemical impact of CO₂ storage in the Surat Basin – Interim report

ANLEC R&D Ref No: 3-1110-0088

Ralf R. Haese, Kyle Horner, Dirk Kirste, Eric Tenthorey and Micaela Grigorescu

June 2013 | CO2CRC Report No: RPT13-4334

REPORT

STUDIES IN CCS



CO2CRC PARTICIPANTS

Core Research Participants

CSIRO
Curtin University
Geoscience Australia
GNS Science
Monash University
Simon Fraser University
University of Adelaide
University of Melbourne
University of New South Wales
University of Western Australia

Industry & Government Participants

ANLEC R&D
BG Group
BHP Billiton
BP Developments Australia
Brown Coal Innovation Australia
Chevron
Dept. of Primary Industries - Victoria
Ministry of Science and Innovation
INPEX
KIGAM
NSW Government Dept. Trade & Investment
Rio Tinto
SASOL
Shell
Total
Western Australia Dept. of Mines and Petroleum
Xstrata Coal

Supporting Participants

CanSyd Australia
Charles Darwin University
Government of South Australia
Lawrence Berkeley National Laboratory
Process Group
The Global CCS Institute
University of Queensland



An Australian Government Initiative



**Regional stress and predicted
hydrogeochemical impact of CO₂ storage
in the Surat Basin – Interim report**

ANLEC R&D Ref No: 3-1110-0088

**Ralf R. Haese, Kyle Horner, Dirk Kirste, Eric Tenthorey and
Micaela Grigorescu**

June 2013

CO2CRC Report No: RPT13-4334



Acknowledgement

The authors wish to acknowledge financial assistance provided to the CO2CRC by the Australian Government through its CRC program and through Australian National Low Emissions Coal Research and Development (ANLEC R&D). ANLEC R&D is supported by Australian Coal Association Low Emissions Technology Limited and the Australian Government through the Clean Energy Initiative.

Cooperative Research Centre for Greenhouse Gas Technologies (CO2CRC)

GPO Box 463
Ground Floor NFF House, 14-16 Brisbane Avenue, Barton ACT 2600
CANBERRA ACT 2601
Phone: +61 2 6120 1600
Fax: +61 2 6273 7181
Email: info@co2crc.com.au
Web: www.co2crc.com.au

Reference: **Haese, R, Horner, K, Kirste, D, Tenthorey, E and Grigorescu, M**, 2013. *Geochemical impacts and monitoring of CO₂ storage in low salinity aquifers*. Cooperative Research Centre for Greenhouse Gas Technologies, Canberra, Australia, CO2CRC Publication Number RPT13-4334. 37pp.

© CO2CRC 2013

Unless otherwise specified, the Cooperative Research Centre for Greenhouse Gas Technologies (CO2CRC) retains copyright over this publication through its incorporated entity, CO2CRC Ltd. You must not reproduce, distribute, publish, copy, transfer or commercially exploit any information contained in this publication that would be an infringement of any copyright, patent, trademark, design or other intellectual property right.

Requests and inquiries concerning copyright should be addressed to the Communications and Media Adviser, CO2CRC, GPO Box 463, CANBERRA, ACT, 2601. Telephone: +61 2 6120 1600.

Executive summary

This interim report of the project *Geochemical Impacts and Monitoring of CO₂ Storage in Low Salinity Aquifers* summarises the work progress to date and initial research findings. The project addresses strategic research questions about CO₂ storage in low salinity aquifers, for example, whether and how subsurface hydrochemical monitoring can be most effective. It uses as a case study the Surat Basin, where low-salinity formation water is found in the prospective CO₂ storage reservoirs. Two specific geochemical objectives are addressed: Firstly, fluid-rock reactions under CO₂ storage conditions are studied through modelling and batch experiments to determine the extent of fluid and mineral trapping capacity and to identify hydrochemical monitoring indicators. Secondly, a coupled transport-reaction model involving co-contaminants such as SO₂, NO₂, and O₂ is developed to better constrain potential risks associated with the co-injection of flue gases in addition to CO₂. Additionally, the project derives stress field data and draws initial conclusions on mechanical seal integrity under CO₂ storage conditions in the Surat Basin as this has been identified an important knowledge gap.

The Precipice Sandstone is the primary prospective CO₂ storage reservoir of the Surat Basin. It is a high porosity / high permeability sandstone with a thickness of 38 meters at the reference well site, GSQ Chinchilla 4. The mineralogy is dominated by quartz with minor amounts (< 35 weight%) of kaolinite and trace amounts (< 1 weight%) of feldspars and clay minerals including illite and chlorite. CO₂-water-rock reaction path modelling has been undertaken with using formation mineralogy and initially CO₂-saturated formation water. Rock reactivity of the Precipice Sandstone is generally very low with kaolinite being the most abundant newly formed mineral. The net change in pore volume is negligible. The Hutton Sandstone, a secondary reservoir situated above the Precipice Sandstone and its sealing unit, the Evergreen Formation, exhibits more variable mineralogy. While still predominantly composed of quartz, the Hutton Sandstone includes greater proportions of reactive mineral phases such as albite, chlorite, and calcite than the Precipice Sandstone.

Kinetic geochemical model results indicate that when SO₂ is introduced as a co-contaminant and allowed to disproportionate in solution forming sulphuric acid, calcite dissolves very quickly and serves as a pH buffer. In the presence of SO₂, anhydrite is predicted to form at the expense of calcite without considerable change in the net porosity. Based on these initial observations, the mineral trapping capacity for CO₂ in the Surat Basin is very low. The CO₂ fluid trapping rate was estimated using an analytical solution, but the results are not convincing. Further work will be undertaken to better constrain this process.

Horizontal stress field data from 30 sites within the Surat Basin have been added to the pre-existing three sites as published in the Australasian Stress Map. In the northern Surat Basin, the maximum horizontal stress is approximately E-W, while further to the south the stress rotates to a more N-S direction. The vertical stress is consistently in the range of 20-22 MPa km⁻¹ and the minimum horizontal stress is estimated as 20 MPa km⁻¹. The maximum horizontal stress is most difficult to estimate and ranges here between 20 and 38 MPa km⁻¹.

Table of contents

Executive summary	i
Table of contents	ii
Figures	ii
Tables.....	iv
1. Introduction	1
2. Sample locations and lithostratigraphy.....	2
3. Predicting the fluid and mineral trapping capacity	6
3.1. Introduction	6
3.2. Estimating the fluid trapping capacity	6
3.2.1. Calculating CO ₂ (molecular) diffusive flux across the scCO ₂ – water interface	8
3.2.2. Calculating the plume outer area.....	9
3.2.3. Comparison of dissolved and injected CO ₂	10
3.3. Estimating the mineral trapping capacity	14
3.3.1. Equilibrium Mineral Trapping Modelling	15
3.4. Discussion	18
4. Modelling the reactive transport of CO₂ and co-contaminants.....	19
4.1. Geochemical modelling.....	19
4.2. Modelling results	21
4.2.1. Precipice Sandstone.....	22
4.2.2. Hutton Sandstone	24
4.3. Discussion	27
5. The regional stress field and implications for fault stability.....	28
5.1. Introduction	28
5.2. New data	29
5.3. Results and discussion	30
6. Conclusions.....	34
7. References	35

Figures

Figure 1: The Surat Basin with key structural geological features, locations of cores used to determine the mineral composition of lithological units of interest, the Greenhouse Gas (GHG) EPQ7 tenement and core locations used in this study.	2
Figure 2: Generalised stratigraphic section for the prospective Jurassic-age reservoir-seal pairs in the Surat Basin. Figure from Farquhar et al. 2013.	3
Figure 3: Lithology with new derived stratigraphic boundaries (SB) from the base of the Precipice Sandstone to the top of the Evergreen Formation in core GSQ Chinchilla 4.....	4
Figure 4: Lithology with new derived stratigraphic boundaries (SB) from the base of the Precipice Sandstone to the top of the Evergreen Formation in core GSQ Roma 8.....	5
Figure 5: Maximum CO ₂ solubility for Precipice Sandstone formation waters over the range of temperature, salinity, and total pressure observed in the Surat Basin. Figure A. illustrates solubility in a typical low-salinity formation water (TDS = 503 mg/L) and Figure B. illustrates CO ₂ solubility in a higher-salinity water (TDS = 3356 mg/L).....	7
Figure 6: Simulated pH of Precipice Sandstone formation waters at equilibrium with a potential range of CO ₂ (aq). Bottom curves illustrate pH in low-salinity formation waters (TDS = 503 mg/L) and top curves illustrates pH in high-salinity waters (TDS = 3356 mg/L).....	8

Figure 7: CO ₂ (aq) depth profiles (A.) and the accumulation of CO ₂ (aq) below the CO ₂ plume over time (B.)	9
Figure 8: Modelled evolution of the plume radius for the Precipice Sandstone at the GSQ Chinchilla 4 site over 30 years of injection (A.). The gradual increase in injection rate over 1.25 years is followed by a constant injection rate of 2.49 million tonnes CO ₂ per year (B.). Other conditions are described in the text.	10
Figure 9: Comparison of the CO ₂ mass dissolved (A.) and injected (B.) with time. Note the difference in scale on the y-axis.	11
Figure 10: Critical time, t_c , the thickness of the CO ₂ enriched layer, δ_c , and the critical wavelength, λ_c , as a function of permeability, k , with $\Delta\rho = 5\text{kg m}^{-3}$, $\phi = 0.3$, $\mu = 0.005\text{ Pa}$ and $D_{\text{sed}} = 10^{-9}\text{ m}^2\text{s}^{-1}$ (Riaz et al., 2006).....	12
Figure 11: Calculated CO ₂ dissolution during the injection period. Note, this rate is likely significantly too low and requires further investigations (see text).....	12
Figure 12: Linear correlation between the CO ₂ (aq) concentration and the increase in fluid density (Li et al. 2011).....	13
Figure 13: High resolution two-dimensional representation of the $\Delta\rho$ distribution with fluid flow direction and velocity (arrows) during convective mixing. Dark red and dark blue represent highest and lowest $\Delta\rho$ values, respectively (from Pau et al. 2010).	13
Figure 14: Change in carbonate saturation during Precipice Sandstone reaction with CO ₂ saturated high salinity (TDS= 3356 mg/L) formation water at 60°C and 80 Bar.	17
Figure 15: Change in carbonate saturation during Hutton Sandstone reaction with CO ₂ saturated high salinity (TDS= 3013 mg/L) formation water at 60°C and 80 Bar.	17
Figure 17: Reaction path modelling outcome for the Precipice Sandstone sample 1190 using the low salinity Precipice formation water.	23
Figure 18: Reaction path modelling outcome for the Precipice Sandstone sample 1190 using the higher salinity Precipice formation water with CO ₂ only.	23
Figure 19: Reaction path modelling outcome for the Precipice Sandstone sample 1190 using the higher salinity Precipice 2 formation water with CO ₂ and SO ₂	25
Figure 20: Reaction path modelling outcome for the Hutton Formation sample 848 using the lower salinity Hutton 1 formation water composition.	25
Figure 21: Reaction path modelling outcome for the Hutton Formation sample 848 using the higher salinity Hutton 2 formation water composition.	26
Figure 22: Reaction path modelling outcome for the Hutton Formation sample 848 using the higher salinity Hutton 2 formation water composition with CO ₂ and co-contaminant SO ₂	26
Figure 23: Horizontal stress measurements currently available for eastern Queensland (http://www.asprg.adelaide.edu.au/asm/). Arrows show the orientation of the maximum horizontal stress. NF: Normal Fault, SS: Strike-Slip Fault, TF: Transverse Fault, U: Undetermined. Note, how limited information is available for the Surat Basin.	28
Figure 24: New stress orientation information available for the Surat Basin, as interpreted from borehole breakouts and drilling induced tensile fractures in wells. Arrows indicate the orientation of the maximum horizontal stress. Red arrows: new stress data interpreted in this study, Green arrows: stress data provided by Brooke-Barnett et al (2012), Blue arrow: unknown Roma well of Khaksar et al. (2012), Orange arrow: from Johnson et al. (2010), Black arrows: previous available stress data from the Australasian Stress Map Database.	29
Figure 25: Vertical stress profile for four wells acquired by integrating density logs over depth. Results are consistent with each other and suggest that the vertical stress magnitude is between 20-22 MPa km ⁻¹	31

Tables

Table 1: Representative formation water composition used for geochemical modelling. Concentrations in mg/Kg.....	7
Table 2: Input values for the calculation of CO ₂ accumulation relevant to the Precipice sandstone using Eq. 2. Dw-CO ₂ from Schulz (2006).....	9
Table 3: Representative LPNORM calculated mineral amounts in weight %.	14
Table 4: Modelled mineralogical composition of system following equilibrium titration of 100 kg of Hutton Sandstone (848.2m) to 10 kg of high-salinity and low-salinity formation waters at 60°C and a fixed pCO ₂ =10 ^{-1.5} bar. Mineral mass given in kg.	16
Table 5: Equilibrated formation water composition in mg/kg.....	22
Table 6: Surat wells containing image logs that provide information on the orientation of the maximum horizontal stress. FMI: Fullbore formation micro-imager, UBI: Ultrasonic borehole imager, CMI: Compact micro-imager.	30
Table 7: Minimum horizontal stress values acquired at various wells in the Surat Basin.	32

1. Introduction

Deep aquifers in sedimentary basins offer great potential capacity for CO₂ storage as they are often tens to hundreds of meters thick, they extend laterally over hundreds of kilometers and the porosity often ranges between 5 and 25% or more. CO₂ is most efficiently stored where it reaches high density at depths >800 m where it is present in supercritical phase. Globally, most deep aquifers contain saline water (~30–50 g/L total dissolved solid, TDS) or brine (> 50 g/L TDS); therefore, international research has typically been directed towards a better understanding of CO₂ storage conditions in saline aquifers.

The Great Artesian Basin (GAB) is Australia's largest groundwater system, extending over several sedimentary basins including the Permo-Triassic Bowen and Galilee basins and the Jurassic Surat and Eromanga basins. The groundwater of the Great Artesian Basin is consistently fresh to brackish with TDS concentrations below 5 g/L (Herczeg et al., 1991). Not only do the strata that make up the GAB host conventional oil and gas, tight gas, minable coal, and coal seam gas resources, but they may provide the potential for CO₂ injection and storage. However, the lower-than-normal TDS concentration affect the CO₂ storage conditions in the basin by, for example, influencing CO₂ solubility (Duan and Sun 2003) and water density (Duan et al. 2008) and thereby affecting the fluid trapping capacity. Additionally, water acidity (pH) is controlled by the degree of CO₂ saturation and may affect the rate of dissolution of some minerals, leading to the mobilisation of cations. Following the addition of CO₂, elements such as calcium, magnesium and iron may later precipitate out of formation waters as carbonate minerals at higher pH conditions, contributing to mineral trapping capacity. These points outline aspects of carbon storage in low TDS aquifers that are of particular importance in Australia and require further investigation.

Three objectives are addressed with this study. Firstly, the lack of an understanding of geochemical impacts of CO₂ storage under freshwater conditions is one motivation for this study. The high concentrations of CO₂(aq) at saturation and associated low pH under low salinity conditions impose major changes in the water composition within an injection field site. Such circumstances are explored in this study with the aim to estimate fluid and mineral trapping capacity and to derive water quality indicators for sub-surface monitoring purposes. While these research objectives are generic, they have immediate applications for the assessment of storage conditions in the Surat Basin. This basin has been rated very suitable for CO₂ storage (Carbon Storage Taskforce 2009) and, therefore, serves as a case study in this project. Secondly, it has been proposed to co-inject flue gases containing compounds other than pure CO₂ such as SO_x, NO_x and O₂ in order to minimise the costs of gas purification. The introduction of these co-contaminants into the reservoir has implications for storage conditions as these gases are reactive and may impose significant changes in the fluid and mineral composition of the reservoir, even at low concentrations. To assess the potential geochemical impacts of injecting co-contaminants, this study is developing a coupled reactive-transport model using input parameters from the Surat Basin to simulate the transport and reactivity of CO₂ together with other gases. Thirdly, this study addresses one aspect of seal integrity of the Evergreen Formation overlying the Precipice Sandstone, the potential storage reservoir in the basin, by assessing the fault orientation relative to the regional stress field and the implications for potential fault reactivation and vertical transmissivity. This geophysical study is being undertaken at a "whole-of-basin" scale.

2. Sample locations and lithostratigraphy

An overview of the Queensland portion of the Surat Basin is shown in Figure 1. Major towns, the EPQ7 greenhouse gas tenement area, locations of rock cores from Geological Survey of Queensland (GSQ) wells GSQ Chinchilla 4 and GSQ Roma 8 and major structural elements are illustrated.

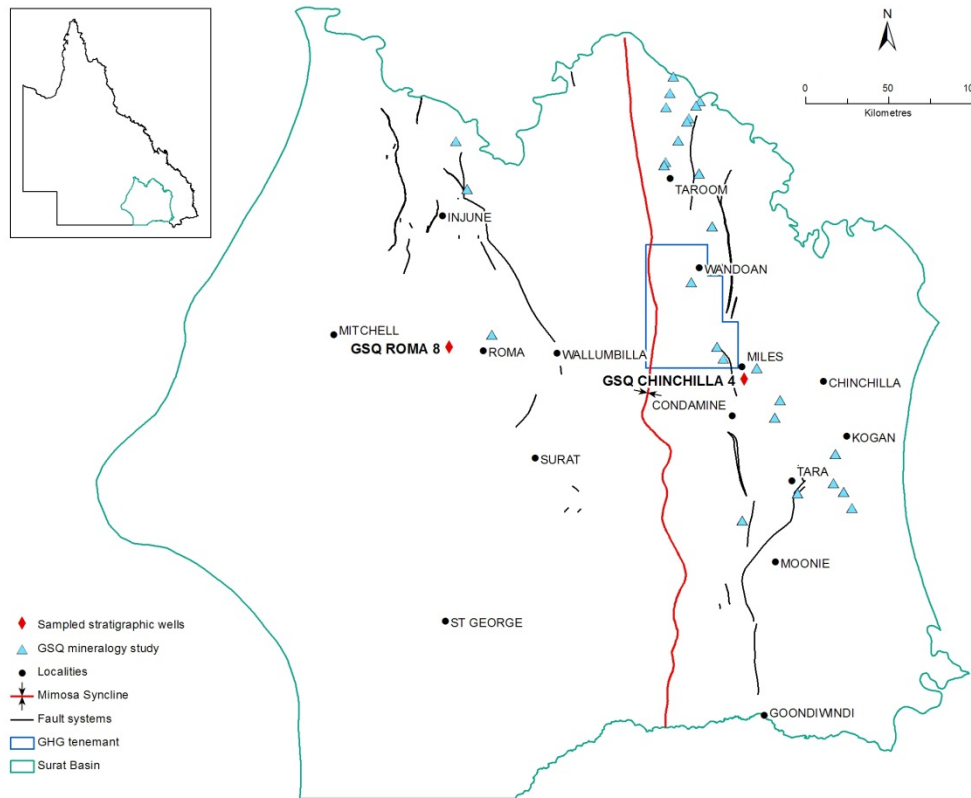


Figure 1: The Surat Basin with key structural geological features, locations of cores used to determine the mineral composition of lithological units of interest, the Greenhouse Gas (GHG) EPQ7 tenement and core locations used in this study.

Cores GSQ Chinchilla 4 and GSQ Roma 8 provide key information, particularly in terms of lithology and lithostratigraphy for this study. A generalised stratigraphic section for the prospective reservoir and seal pairs in the Surat Basin is presented in Figure 2. The detailed lithology and the derived lithostratigraphy of the two cores examined in this study are shown from the base of the Precipice Sandstone to the top of the Evergreen in Figures 3 and 4. Rock properties relevant for this study such as porosity, permeability and mineralogy have been reported previously (Haese et al. 2013).

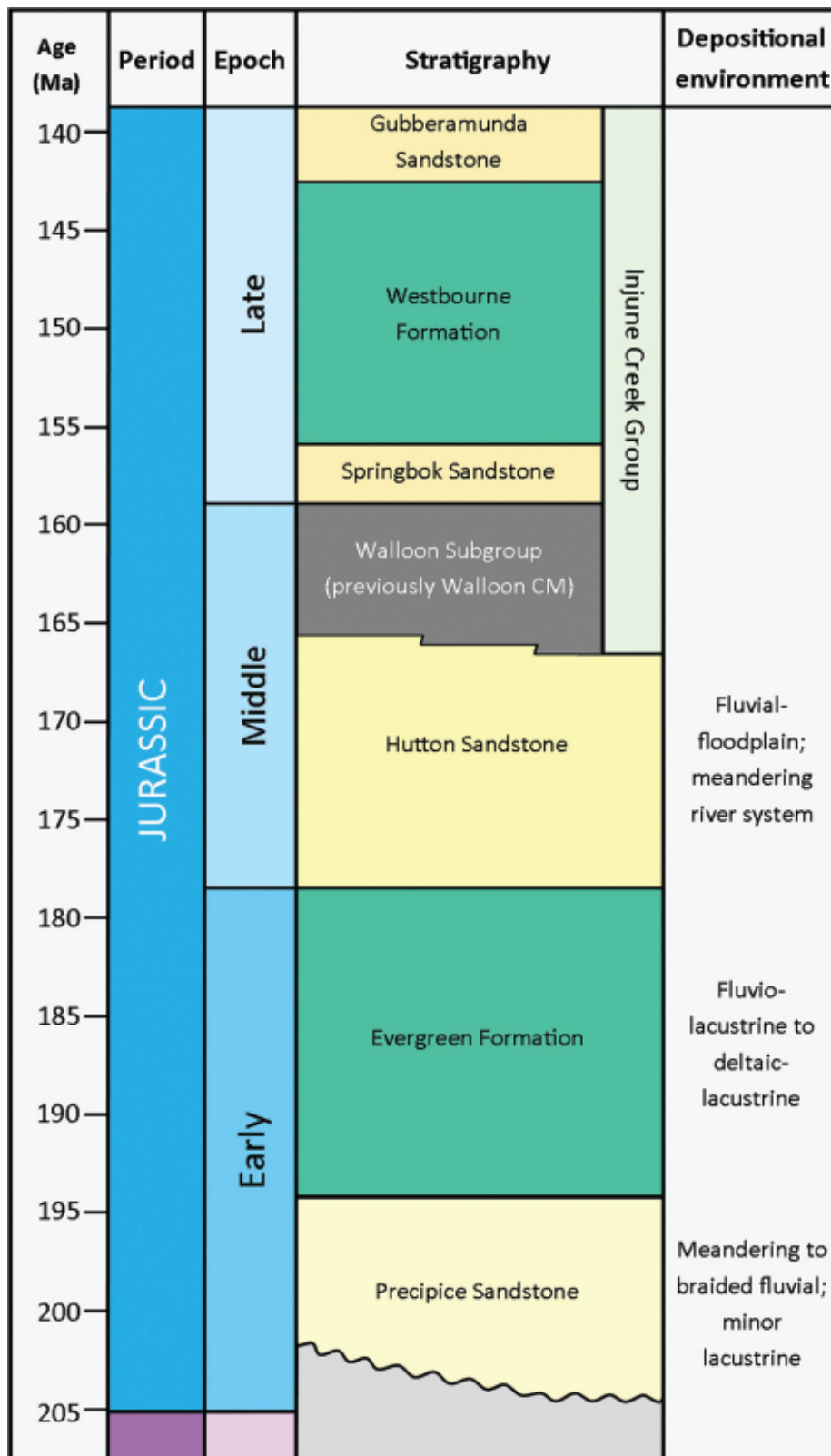


Figure 2: Generalised stratigraphic section for the prospective Jurassic-age reservoir-seal pairs in the Surat Basin. Figure from Farquhar et al. 2013.

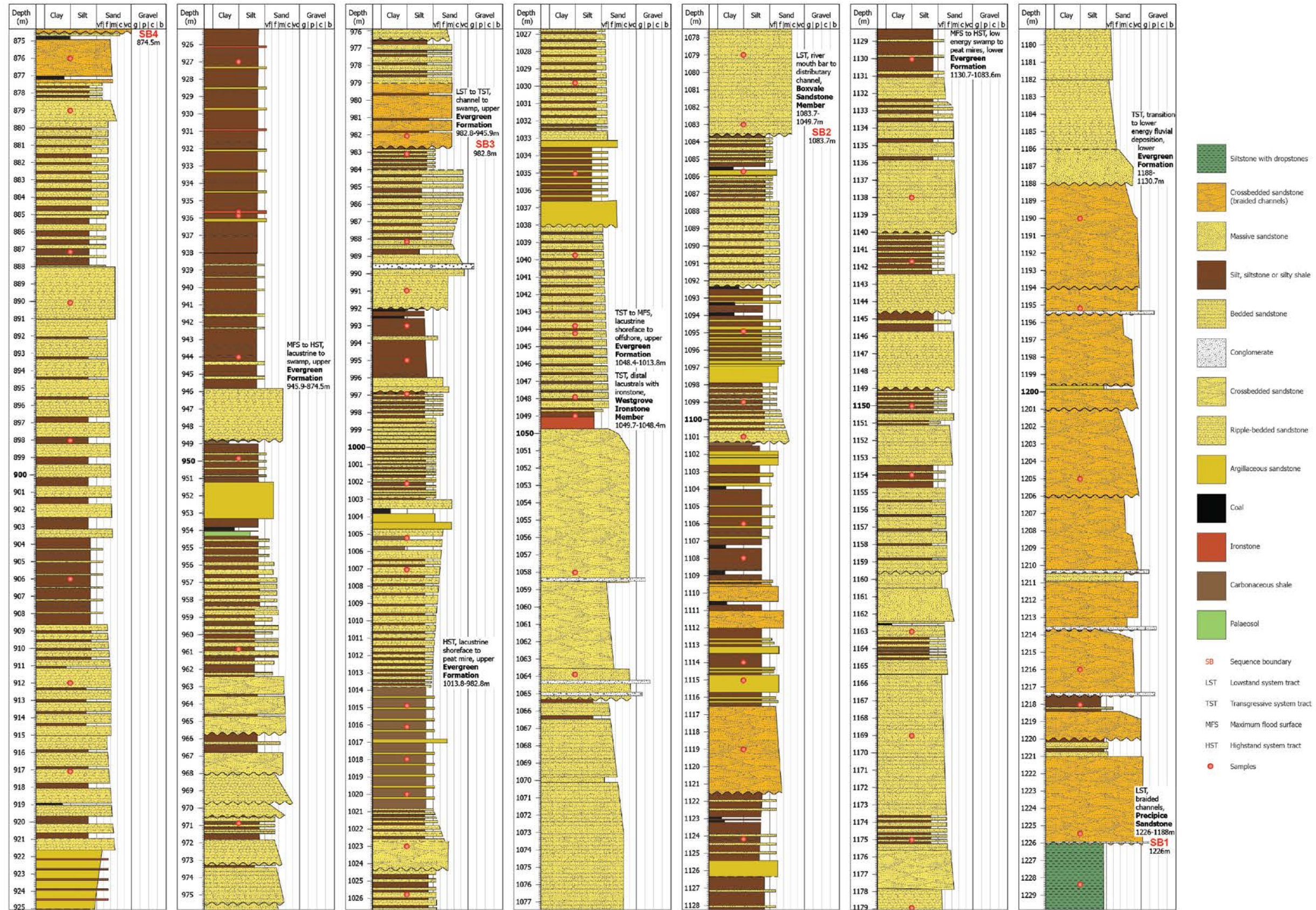


Figure 3: Lithology with new derived stratigraphic boundaries (SB) from the base of the Precipice Sandstone to the top of the Evergreen Formation in core GSQ Chinchilla 4.

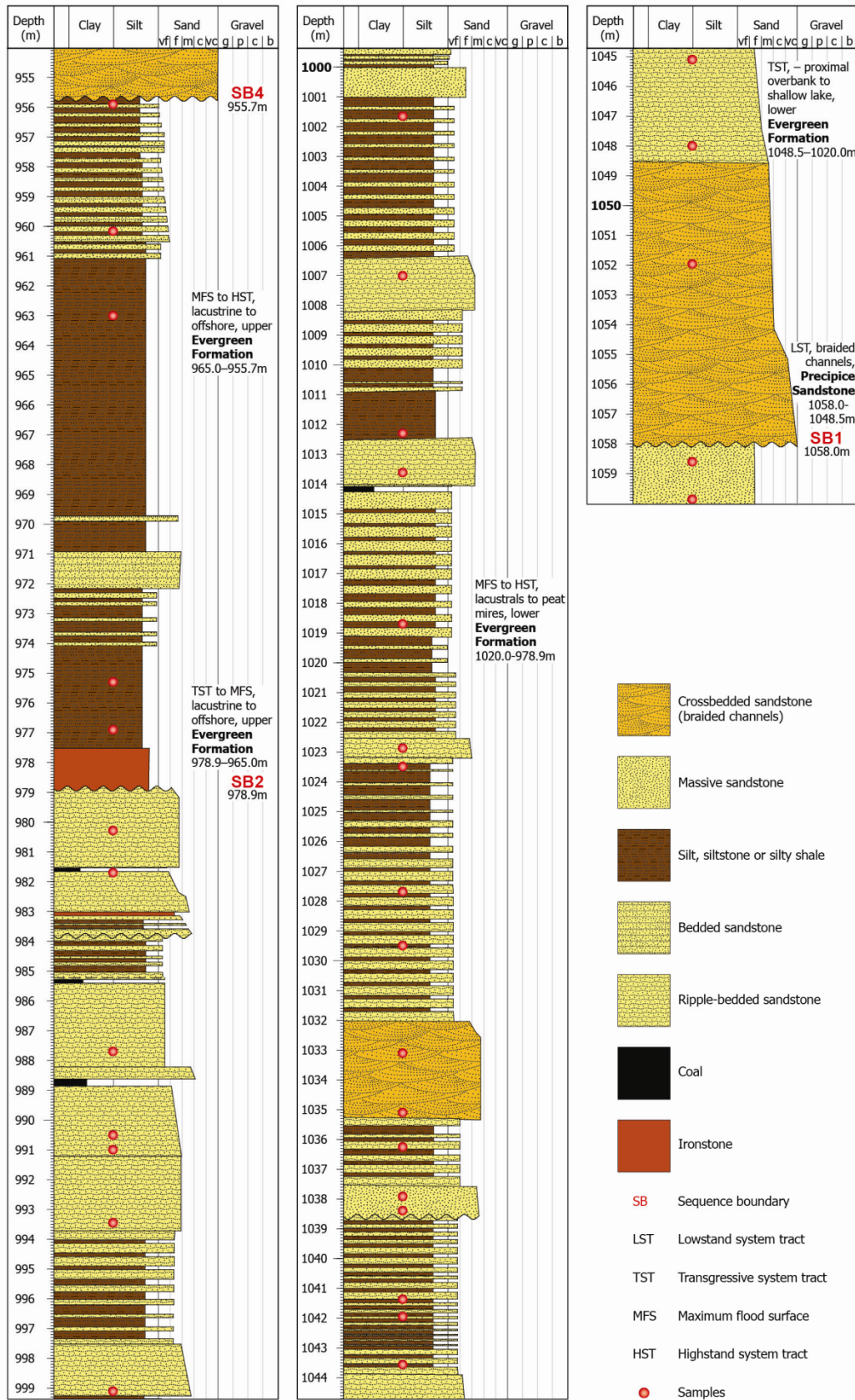


Figure 4: Lithology with new derived stratigraphic boundaries (SB) from the base of the Precipice Sandstone to the top of the Evergreen Formation in core GSQ Roma 8.

3. Predicting the fluid and mineral trapping capacity

3.1. Introduction

CO₂ is stored in a reservoir by four different trapping mechanisms:

1. Structural trapping where CO₂ is contained from moving vertically to the surface by an overlying aquitard.
2. Residual trapping where supercritical CO₂ is trapped in the pores between sediment grains.
3. Fluid trapping where CO₂ is dissolved in the formation water.
4. Mineral trapping where carbon is immobilised through the formation of carbonate minerals.

Fluid trapping is considered one of the safest ways of CO₂ storage because the CO₂ enriched fluid has an increased density and slowly sinks to the bottom of the reservoir and water is generally less mobile than supercritical CO₂, scCO₂. The maximum fluid trapping capacity is effectively the CO₂ solubility, which depends on pressure, temperature and total dissolved solid concentration of the formation water. However, because the CO₂ enriched fluid starts migrating downward before the CO₂ saturation concentration is reached (Gasda et al. 2011), one needs to estimate the actual fluid trapping rate by modelling the CO₂ dissolution coupled to convective mixing (Ennis-King and Paterson 2003, Gasda et al. 2011). Critically important for the outcome of such a modelling study is an appropriate representation of the reservoir heterogeneity. For example, at the Sleipner CO₂ storage site, approximately ten inter-bedded thin siltstone layers have resulted in vertically stacked layers of scCO₂ within the reservoir leading to a very high CO₂ fluid trapping rate equivalent to approximately 10% of the injection rate (Neufeld et al. 2010).

Mineral trapping is the safest way to store CO₂, because carbonate mineral precipitation leads to the complete immobilisation of the injected carbon. Estimating the mineral trapping capacity involves the modelling of fluid-rock interactions with input parameters such as the mineralogy, the reactive surface area of minerals in major lithological units and the water composition of the reservoir. If one considers the reservoir as a closed system isolated from adjacent formations this modelling is relatively straight forward and allows a first-pass estimate of the mineral trapping capacity at different stages of water-rock-CO₂ reaction. However, more accurate predictions of the rate of carbonate mineralisation with time require a coupled reactive transport model utilising a geological model.

3.2. Estimating the fluid trapping capacity

Maximum CO₂ solubility in formation waters was calculated using the solubility model of Duan et al. (2006). The calculations take into account TDS, gas fugacity, and formation temperature and pressure on the solubility of CO_{2(g)} in formation waters. Reaction temperature was set between 25°C and 60°C, and CO_{2(aq)} solubilities were calculated for a range of CO₂ partial-pressures between 10^{-1.5} bar (pre-injection conditions inferred from Coudrain-Ribstein et al. (1998)) to 100 bar (post-injection conditions at formation pressure). Formation water compositions used in this study are taken from Hodgkinson et al. (2010), Grigorescu (2011b) and Hodgkinson and Grigorescu (2012), as well as a joint GA/GSQ survey conducted between 2009 and 2011 (Table 1).

Table 1: Representative formation water composition used for geochemical modelling. Concentrations in mg/Kg.

Formation	TDS	Na	Ca	Mg	K	Cl	SO4	SiO2	HCO3
Hutton (low salinity)	632	190	1	1	1	120	1	18	300
Hutton (high salinity)	3013	1000	8	1	5	1130	1	18	850
Precipice (low salinity)	503	55	68	30	10	115	50	15	160
Precipice (high salinity)	3356	1100	25	5	25	1170	1	25	1005

Example results for maximum CO₂ solubility in low and high salinity Precipice Sandstone formation waters are illustrated in Figure 5. No significant differences in CO₂ solubility are evident over the range of salinities observed in the reservoir. Rather, formation temperature exerts the greatest control on CO₂ solubility in the Surat Basin. CO₂ solubility is greatest at low formation temperatures, with maximum CO₂ solubility ranging from approximately 1.0 mol L⁻¹ (60°C) to 1.4 mol L⁻¹ (25°C) at 100 Bar, irrespective of water salinity. As temperatures >32°C are required to maintain carbon dioxide in a supercritical state, CO₂ solubilities in the prospective geosequestration reservoirs in the Surat Basin will be less than the maximum values presented in Figure 5.

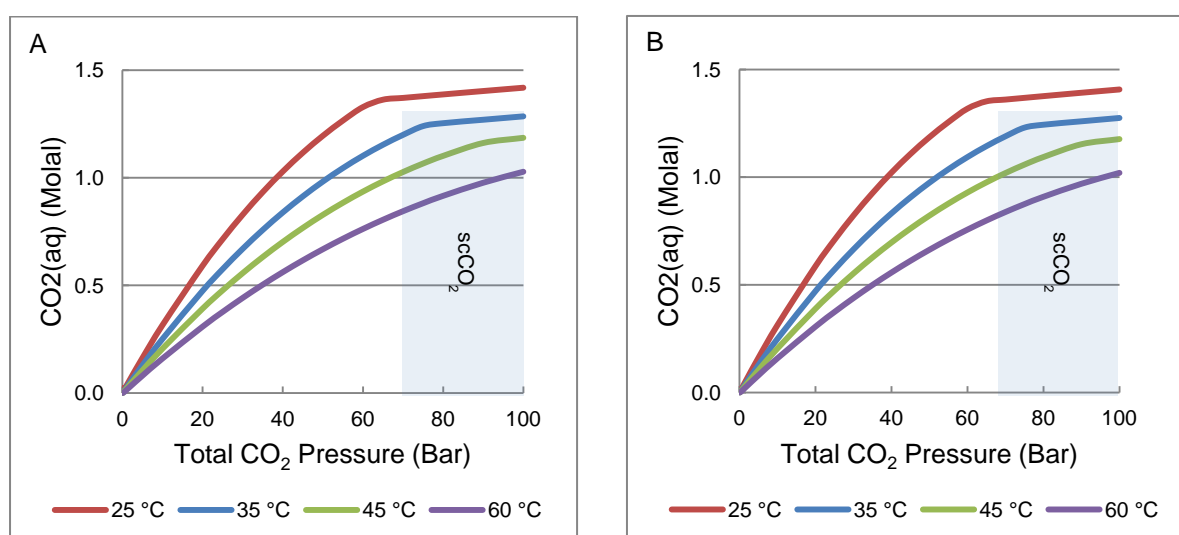


Figure 5: Maximum CO₂ solubility for Precipice Sandstone formation waters over the range of temperature, salinity, and total pressure observed in the Surat Basin. Figure A. illustrates solubility in a typical low-salinity formation water (TDS = 503 mg/L) and Figure B. illustrates CO₂ solubility in a higher-salinity water (TDS = 3356 mg/L).

CO₂ solubility also increases with increasing pressure, exhibiting a more gradual rate of increase at higher pressures. The shape of the CO₂ solubility curves suggests that elevated CO₂ solubility may be sustained in a formation even if pressure decreases modestly as CO₂-saturated water migrates away from the injection point. Increased concentrations of CO₂(aq) in solution will lead to the formation of carbonic acid (H₂CO₃), decreasing solution pH. Figure 6 illustrates the pH values of Precipice Sandstone formation waters in equilibrium with the CO₂(aq) concentrations determined by the solubility model of Duan and Sun (2006).

Despite only minor differences in CO₂ solubility (Figure 5), calculations suggest a difference up to half a pH unit between fresh and more saline formation waters at a given CO₂(aq) concentration (Figure 6). This difference is due to the greater HCO₃⁻ concentrations in saline formation waters (Table 1) increasing the acid buffering capacity compared to fresher waters.

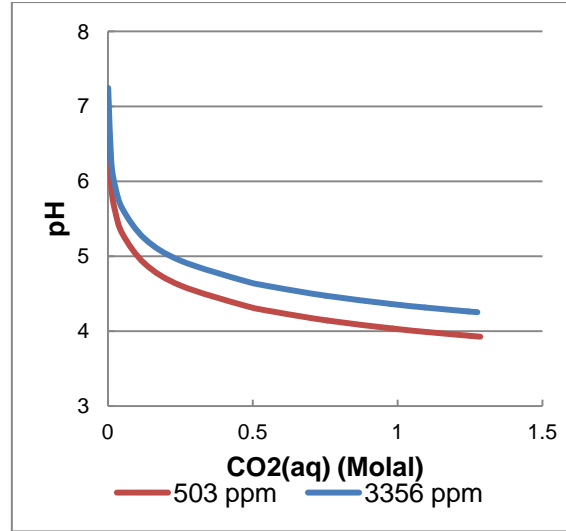


Figure 6: Simulated pH of Precipice Sandstone formation waters at equilibrium with a potential range of $\text{CO}_2(\text{aq})$. Bottom curves illustrate pH in low-salinity formation waters (TDS = 503 mg/L) and top curves illustrates pH in high-salinity waters (TDS = 3356 mg/L).

Assuming an effective porosity of 20%, a temperature of 60°C, and a pressure of 80 bar, calculations suggest that the maximum fluid trapping capacity of Surat Basin formations is approximately 220 mol (9.7 kg) $\text{CO}_2(\text{aq})/\text{m}^3$ of reservoir rock. However, hydrodynamic factors may inhibit formation waters from reaching the maximum calculated $\text{CO}_2(\text{aq})$ concentration during dissolution of supercritical CO_2 .

The rate of CO_2 dissolution changes with time for the following reasons: Firstly, the rate of CO_2 dissolution is initially controlled by molecular diffusion across the scCO_2 -water interface assuming the hydrolysis of $\text{CO}_2(\text{g})$ does not limit the CO_2 dissolution rate. The fluid density increases as a consequence of the CO_2 enrichment within a thin layer beneath the CO_2 plume. After a critical time, the CO_2 enriched and denser fluid layer becomes destabilised and starts to segregate downwards. Secondly, the CO_2 plume volume and the respective plume-water interface area increases during the injection phase allowing for an increase in the diffusive flux area.

The following sections outline the workflow and associated model assumptions necessary to calculate fluid trapping by accounting for changing chemical-physical conditions and determining the net CO_2 dissolution flux over time.

3.2.1. Calculating CO_2 (molecular) diffusive flux across the scCO_2 – water interface

An inexhaustible layer with CO_2 -saturated water, C_{sat} , forms the interface between the scCO_2 plume and the underlying aquifer. The latter has its original formation water composition with the original $\text{CO}_2(\text{aq})$ concentration, C_0 . $\text{CO}_2(\text{aq})$ diffuses from the CO_2 -saturated layer into the below lying reservoir and the resulting change in concentration, ∂C , with depth, x , and time, t , can be calculated according to Fick's second law of diffusion:

$$\frac{\partial C}{\partial t} = D_{\text{sed}} \frac{\partial^2 C}{\partial x^2} \quad (1)$$

with D_{sed} the diffusion coefficient in sediment. D_{sed} is calculated from the diffusion coefficient in water, D_w - CO_2 , using $D_{\text{sed}} = D_w \cdot \text{CO}_2 / \theta^2$, with the tortuosity, θ , calculated as a function of porosity, ϕ , $\theta^2 = 1 - \ln(\phi^2)$.

The analytical solution of Eq. 1 is

$$C_{x,t} = C_o + (C_{sat} - C_o) \cdot \operatorname{erfc} \left\{ \frac{x}{2 \cdot \sqrt{D_{sed} \cdot t}} \right\} \quad (2)$$

Full account of Fick's second law of diffusion, its analytical solution and its application in sediments can be found in Schulz (2006).

Table 2 shows values used for the calculation of CO₂ concentrations as a function of depth and time using Eq. 2. Depths were implemented as a column of vertical cells with 10 cells for the top 1 mm, 10 cells for the following 1 cm, 10 cells for the following dm and cells of 10cm further below.

Table 2: Input values for the calculation of CO₂ accumulation relevant to the Precipice sandstone using Eq. 2. Dw-CO₂ from Schulz (2006).

C _{sat}	1 mol L ⁻¹
C ₀	0.0034 mol L ⁻¹
D _w -CO ₂ at 50 °C	2.8 10 ⁻⁹ m ² s ⁻¹
φ	0.2

Figure 7A shows the change in CO₂(aq) profile with time. The CO₂(aq) gradually penetrates deeper into the sediment, whereby the concentration gradient flattens. As a consequence, the CO₂(aq) diffusive flux decreases and the depth-integrated CO₂ enrichment slows down with time (Figure 7B).

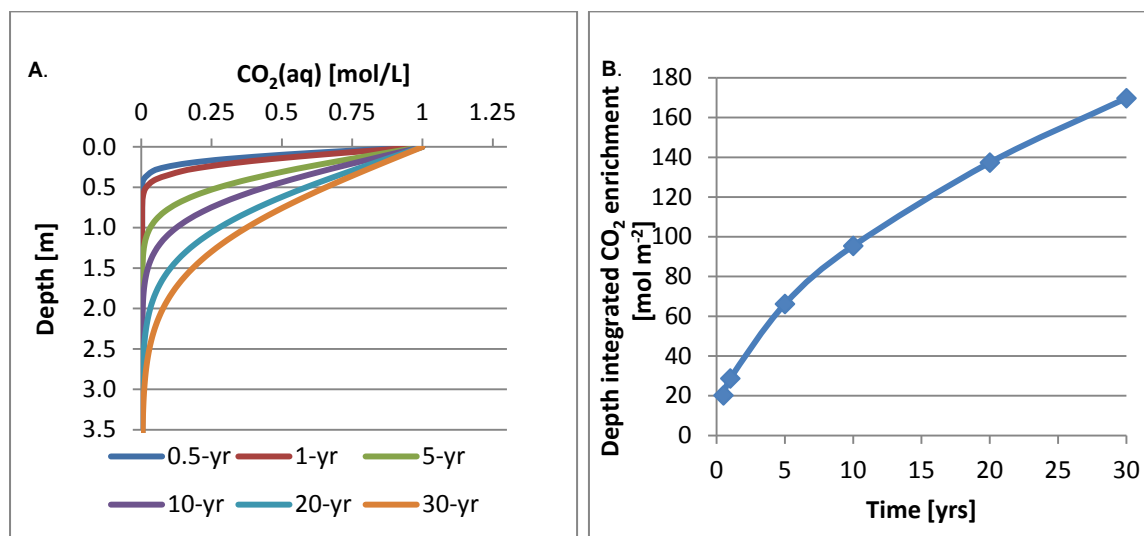


Figure 7: CO₂(aq) depth profiles (A.) and the accumulation of CO₂(aq) below the CO₂ plume over time (B.).

3.2.2. Calculating the plume outer area

After having calculated the diffusive CO₂(aq) accumulation per m², the outer plume area is now estimated using a semi-analytical solution for calculating the plume geometry and pressure in a homogenous and isotropic reservoir (Vilarrasa et al. 2013). Multiplying rates of area-normalised CO₂ accumulation and the estimated outer area of the plume yields CO₂ trapping rates at different times. An Excel spread sheet prepared by Vilarrasa et al. was modified to calculate changes in the plume geometry over 30 years within the Precipice Sandstone under conditions found at the GSQ Chinchilla 4 site. All of the input data by Vilarrasa et al. were used except for the following: The thickness of the reservoir is 36 meters (1188–1224 m depth) and the reservoir is discretised into 25 cells of 1.44 vertical meters. The reservoir temperature is 50°C, the isotropic permeability is 1 Darcy (1·10⁻¹² m⁻²) and the porosity is 0.2.

A cone-shaped curvature of the vertical change in radius was expected rather than the s-shaped curvature shown in Figure 8A. The observed shape is likely related to CO₂ compressibility and buoyancy effects in the injection well leading to a higher injection rate in the upper part of the perforated section. This is an effect which has not been sufficiently accounted for before (Vilarrassa et al., 2013).

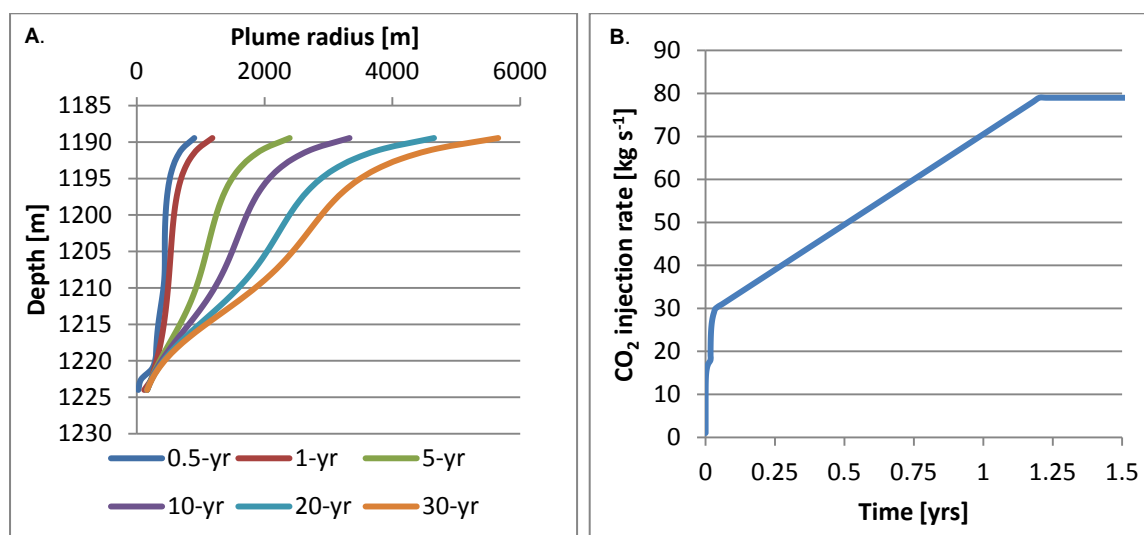


Figure 8: Modelled evolution of the plume radius for the Precipice Sandstone at the GSQ Chinchilla 4 site over 30 years of injection (A.). The gradual increase in injection rate over 1.25 years is followed by a constant injection rate of 2.49 million tonnes CO₂ per year (B.). Other conditions are described in the text.

The area of the plume is estimated as the sum of the outer area of each of the 25 cylindrical cells. As a result, the calculated plume area after 5 years is $0.23 \cdot 10^6$ m², which is more than an order of magnitude lower than the plume area at the Sleipner site (Norway) after six years of injection ($5.6 \cdot 10^6$ m²). This is a particularly striking difference as the injection rate in this hypothetical scenario is 2.5 million tonnes CO₂ per year after the first year (Figure 8B), whereas the average injection rate at the Sleipner site is only ~1 million tonnes CO₂. This discrepancy requires further research to derive accurate plume areas at different times.

3.2.3. Comparison of dissolved and injected CO₂

The dissolved CO₂ plume area was determined by multiplying the depth-integrated CO₂(aq) enrichment at the various calculated time intervals (Figure 9A). This approach yields an overestimate of the CO₂ dissolved at the plume margin as its associated surface area has been in place for a shorter period than assumed in the calculation. However, a comparison of the dissolved and injected CO₂ over time shows the injected CO₂ to be three to four orders of magnitude higher (Figure 9B). Therefore, the CO₂ dissolution rate is negligible when compared to the structural / stratigraphic trapping rate during the injection phase.

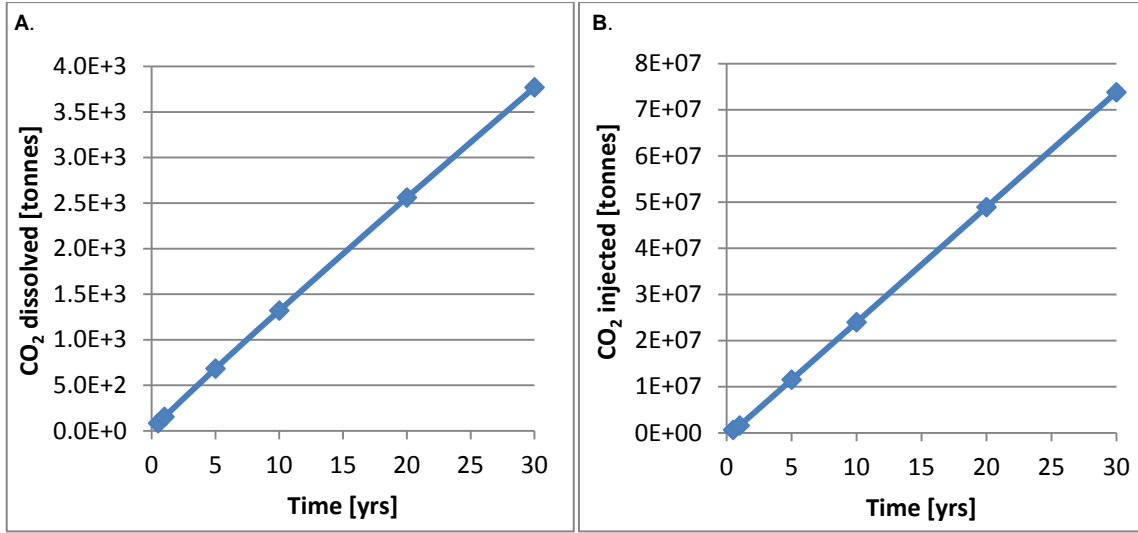


Figure 9: Comparison of the CO₂ mass dissolved (A.) and injected (B.) with time. Note the difference in scale on the y-axis.

As stated previously, the CO₂ enriched fluid layer underneath the CO₂ plume eventually becomes dense enough and starts to segregate downwards. According to Riaz et al. (2006) the CO₂ penetration depth, δ_c , and the critical time, t_c , at the onset of instability can be calculated as

$$\delta_c \approx \frac{24\mu D_{sed}}{K\Delta\rho g} \text{ and} \quad (3)$$

$$t_c = 146 \frac{\phi\mu^2 D_{sed}}{(K\Delta\rho g)^2} \quad (4)$$

with μ the viscosity, $\Delta\rho$ the increase in fluid density, k the permeability and g the gravity acceleration. Independently, Xu et al. (2006) give a very similar equation for t_c ,

$$t_c = C_{I1} \frac{(\phi\mu)^2 D_{sed}}{(K\Delta\rho g)^2} \quad (5)$$

with the constant parameter C_{I1} calculated as 75.19.

Using $\phi = 0.2$, $k = 1$ Darcy ($=10^{-12} \text{ m}^2$), $\mu = 0.005 \text{ Pa s}$, $D_{sed} = 10^{-9} \text{ m}^2 \text{ s}^{-1}$, $\Delta\rho = 10 \text{ kg m}^{-3}$, and $g = 9.81 \text{ m s}^{-2}$ leads to a critical time for the onset of instability after 80 and 8 days according to Eq. 4 and 5, respectively. The estimated depth of the CO₂ enriched water layer at the time of destabilisation is 0.12 meters according to Eq. 3. These results illustrate that the predicted onset of boundary layer destabilisation occurs very quickly after the emplacement of scCO₂ under the conditions prevailing for the Precipice Sandstone at the GSQ Chinchilla 4 site. Note the significant effect of permeability on t_c and δ_c (Figure 10).

The CO₂ dissolution rate after boundary layer destabilisation has to account for convective transport and is given by Neufeld et al. (2010) as:

$$F_{CO_2} [kg \text{ m}^{-2} \text{ y}^{-1}] = \alpha \cdot C_{sat} \cdot \left(\frac{kg\Delta\rho}{\mu}\right)^{4/5} \cdot \left(\frac{D_{sed}\phi}{H}\right)^{1/5} \quad (6)$$

with $\alpha = 0.19$ and C_{sat} expressed as weight fraction.

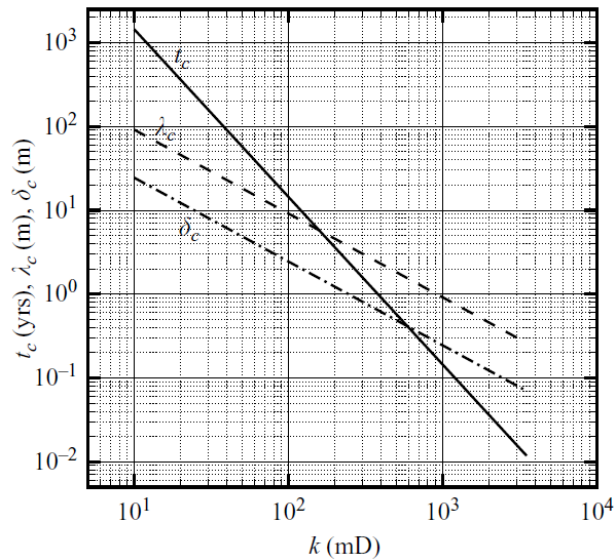


Figure 10: Critical time, t_c , the thickness of the CO₂ enriched layer, δ_c , and the critical wavelength, λ_c , as a function of permeability, k , with $\Delta\rho = 5\text{ kg m}^{-3}$, $\phi = 0.3$, $\mu = 0.005\text{ Pa}$ and $D_{\text{sed}} = 10^{-9}\text{ m}^2\text{s}^{-1}$ (Riaz et al., 2006).

Using the input values applicable for the Precipice Sandstone at the GSQ Chinchilla 4 site (see input values for Eq. 3-5), a CO₂ convective flux of $6.4\text{ kg m}^{-2}\text{ y}^{-1}$ is calculated. This is approximately ten times higher than the diffusive flux after 5 years ($0.58\text{ kg m}^{-2}\text{ yr}^{-1}$). The cumulative CO₂ enrichment is shown in Figure 11. When compared to the CO₂ injection rate (Fig. 9B), the cumulative CO₂ dissolution is approximately 1000 times lower. This is attributed to the significant underestimation of the plume area, which requires further investigation. For comparison, at the Sleipner site the CO₂ dissolution rate is estimated to be 10% of the injection rate (Neufeld et al., 2010).

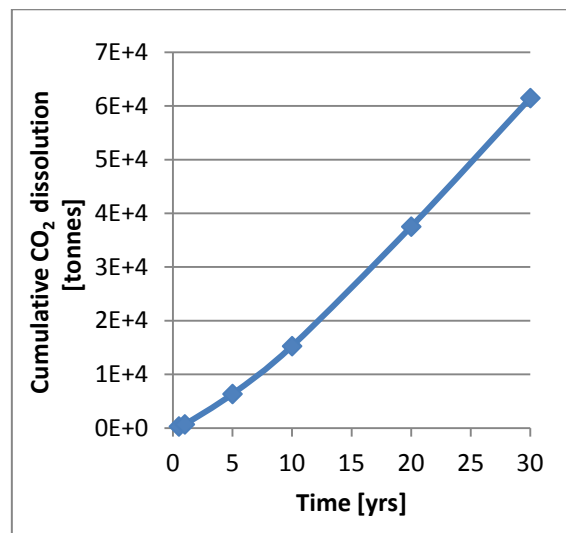


Figure 11: Calculated CO₂ dissolution during the injection period. Note, this rate is likely significantly too low and requires further investigations (see text).

Equations (3) to (6) include $\Delta\rho$, the increase in fluid density related to the increase in CO₂(aq). Several models have been proposed for the relation between CO₂(aq) and fluid density. Here we use a recent one by Li et al. (2011). At 1000 m depth, 50°C and a NaCl concentration of 0.58 mol kg^{-1} (34 g/L), a linear function can be derived (Figure 12). A value of $\Delta\rho = 10\text{ kg m}^{-3}$ for the density increase is found in some studies (Xu et al 2006, Neufeld et al. 2010, Pau et al. 2010), which assumes CO₂ saturation is reached in the destabilised water layer. Gasda et al. (2011) point out the

maximum density increase and respective CO₂ enrichment is only found in the core of the downward advecting fingers and they estimate an average CO₂ mass fraction of only 2% as compared to a maximum of 5%.

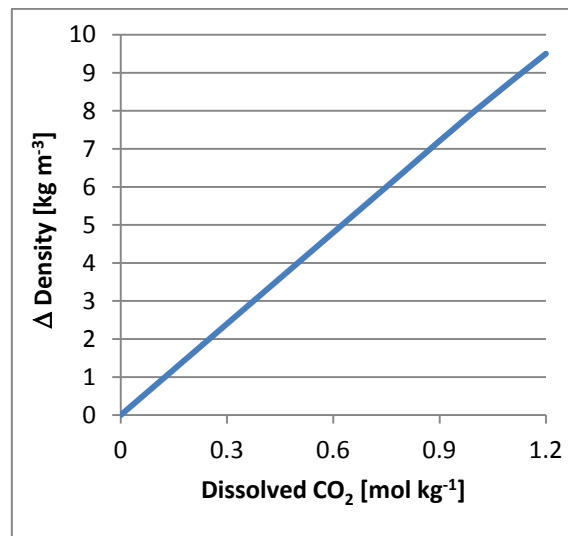


Figure 12: Linear correlation between the CO₂(aq) concentration and the increase in fluid density (Li et al. 2011).

Two-dimensional variation in fluid density during convective mixing is shown in Figure 13. As a consequence of the spatial and temporal variability in CO₂ enrichment, mineral dissolution rates will vary accordingly.

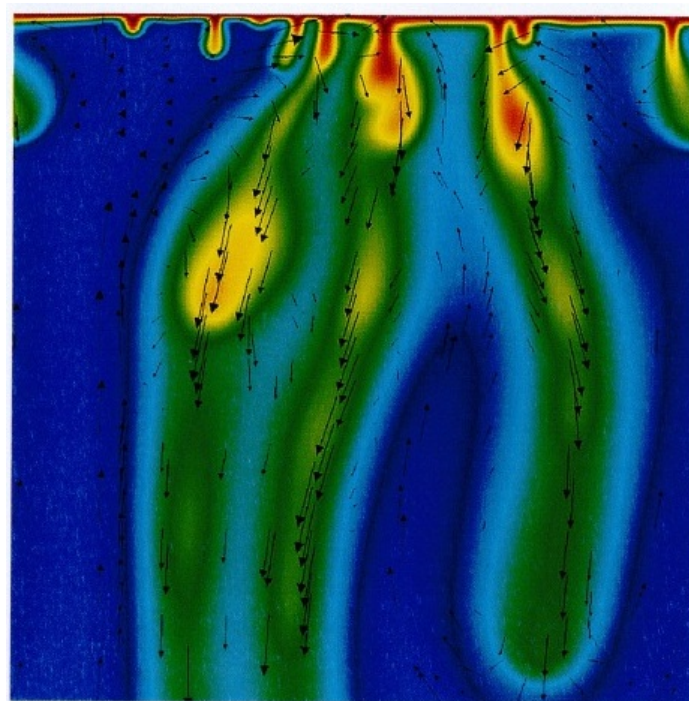


Figure 13: High resolution two-dimensional representation of the $\Delta\rho$ distribution with fluid flow direction and velocity (arrows) during convective mixing. Dark red and dark blue represent highest and lowest $\Delta\rho$ values, respectively (from Pau et al. 2010).

3.3. Estimating the mineral trapping capacity

Geochemical modelling entails a comprehensive accounting of elements that details the reactions between the mineral phases, the aqueous phase and the supercritical CO₂ phase. Mass exchange processes between the different phases are modelled by computer codes utilising thermodynamic and kinetic databases and rate equations, and with accurate information on the minerals and fluid composition present in the studied system. The mineralogy defines the chemical composition of the solid phases and thus is a critical component of the geochemical model.

For this study, 35 core samples from Geological Survey of Queensland (GSQ) stratigraphic well Chinchilla 4 and 16 core samples from well GSQ Roma 8 were collected for detailed physical, mineralogical, and chemical characterisation. Samples were analysed using SEM for microscopic visualisation, thin section petrology, brine injection and gravimetric analysis for permeability and porosity, plus EDS, XRD, XRF, and hyperspectral analysis (Hylogging™) for mineralogical and chemical composition. A summary of lithology and rock properties from the cores is presented in Haese et al. (2013). Results obtained were compared to previously published data for the Surat Basin (Grigorescu 2011a; Farquhar et al. 2013) to ensure samples selected for the geochemical modelling were representative of regional conditions.

To generate a comprehensive mineralogy for use in geochemical models, the XRF can be combined with the results of the other analytical methods through normative analysis (de Caritat et al., 1994). The program LPNORM was used to calculate a best fit mineralogy using the XRD, thin section, SEM and Hylogger semiquantitative mineralogies as constraints. The mineral chemical compositions used in LPNORM are based on the stoichiometric composition from the thermodynamic database, EDS analysis of chlorite (3:1 Fe:Mg) and extinction angle quantitative analysis on plagioclase. Examples of the output of LPNORM analysis for select GSQ Chinchilla 4 core samples are given in Table 3. Normative analysis does not necessarily result in an exact solution for the quantitative mineralogy but it does ensure that the major oxide chemical composition is accounted for in the geochemical models. Additional confirmation of LPNORM mineralogy will come from ongoing refinement of the XRD interpolation and thin section and SEM evaluation. These results can then be used in geochemical models where the total amounts of major elements, and in particular divalent metals, are present and available for reaction while still under the constraints of solubility and reaction rates of the assigned minerals.

Table 3: Representative LPNORM calculated mineral amounts in weight %.

Formation	Hutton	Precipice
Sample ID	848.2	1190
Minerals	wt %	wt %
Quartz (SiO ₂)	38.25	95.61
Albite (NaAlSi ₃ O ₈)	12.95	0.59
K-Feldspar (KAlSi ₃ O ₈)	5.80	
Illite (Al,Mg,Fe Clay)	13.02	0.95
Kaolin (Al ₂ Si ₂ O ₅ (OH) ₄)	22.33	2.46
Chlorite (Fe-rich) (Fe ²⁺ ,Mg) ₅ Al(AlSi ₃ O ₁₀)(OH) ₈	3.59	0.16
Calcite (CaCO ₃)	0.45	
Siderite (FeCO ₃)		0.08
Anatase (TiO ₂)	0.96	0.10
Apatite (Ca ₅ (PO ₄) ₃ (F,Cl,OH)		0.04
Pyrolusite (MnO ₂)	0.01	
Pyrite (FeS ₂)	0.04	0.04
Hematite (Fe ₂ O ₃)	1.28	

3.3.1. Equilibrium mineral trapping modelling

The maximum CO₂ mineral trapping capacity was determined using the aqueous geochemical modelling software The Geochemist's Workbench™ (GWB, Bethke & Yeakel 2013). The extended version of the Lawrence Livermore National Laboratories thermodynamic database, thermo.com.V8.R6+, was used for all calculations. GWB calculates activity coefficients for charged aqueous species using the B-dot equation. The database was modified to calculate the activity coefficient of the neutral aqueous species CO₂(aq), using a truncated form of the polynomial fit of Helgeson (1969) by changing the ion size of CO₂ to -0.5 (see also Section 4). As Surat Basin formation waters have a low salinity (TDS < 5,000 mg/L) minimal salting-out occurred and calculated activity coefficients for CO₂(aq) were near unity throughout all simulations.

Baseline conditions

To characterise pre-injection baseline conditions in the prospective reservoirs, an equilibrium titration model open for CO_{2(g)} (constant gas overhead) was used. A specified mass of formation minerals was added in a stepwise manner to a specified volume of formation water in equilibrium with a fixed CO₂ partial pressure of 10^{-1.5} bar, simulating natural conditions whereby formation water and rock are in contact with an intrinsic formation pCO₂ (estimated from measurements of sedimentary basins summarised by Coudrain-Ribstein et al. (1998)). Geochemical reactions were calculated after each step to assess the geochemical stability of the formation. A mineral/water mass ratio of 10:1 was used in all reaction path models to represent water-saturated sandstone with an effective porosity of 20%.

Precipice Sandstone core samples are typically dominated by the silicate minerals quartz (50 to 100% by mass) and kaolinite (5 to 34% by mass), while interbedded thin shales contain feldspars (albite and K-feldspar) and muscovite (each approximately 10% by mass) as well (Farquhar et al. 2013; Haese et al. 2013). Speciation calculations indicate formation waters under a constant pCO₂ of 10^{-1.5} bar would be saturated or near-saturated for carbonate minerals such as calcite (CaCO₃) and dolomite (CaMg(CO₃)₂). Accordingly, any carbonate cements or minerals present in the Precipice Sandstone under ambient conditions would generally be stable. This is consistent with LPNORM assessment of mineralogical data, which suggests that trace carbonate may be present in the Precipice Sandstone, possibly as cements in the interbedded sandstones. This may also indicate that dissolution of Ca²⁺/Mg²⁺ carbonate or silicate minerals elsewhere along the flow path may be regulating formation water compositions in the Precipice Sandstone.

Equilibrium modelling of Precipice Sandstone formation waters and mineralogy under ambient pCO₂ conditions does not produce a significant change in mineral composition, suggesting formation waters are in equilibrium with the reservoir mineralogy under ambient conditions.

The Hutton Sandstone contains higher proportions of reactive minerals than the Precipice Sandstone, reflected in lower quartz content (40-80%) and higher contents of feldspars such as albite and K-feldspar (Table 3). Carbonate minerals are also more abundant within the Hutton Sandstone (Farquhar et al. 2013; Haese et al. 2013). Sepiolite was identified in the Hutton Sandstone via XRD, but further investigations are warranted to validate this mineral as it is very rarely observed and may well be incorrectly assigned during the initial data analysis. Speciation calculations indicate that low-salinity formation waters in the Hutton Sandstone are slightly undersaturated for almost all minerals except a few clays and iron oxides, and the saline formation water is also saturated for carbonates calcite and dolomite.

The undersaturation of formation waters combined with the presence of soluble minerals suggest water-rock disequilibrium may be common within the unit. This is the case for for all formation waters, as illustrated in Table 4 which summarises the final step of reaction path models titrating Hutton Sandstone (Sample 848.2, Table 2) into low-salinity (TDS=632 mg/L) and high-salinity formation water (TDS = 3013 mg/L) at ambient CO_{2(g)} pressures.

Table 4: Modelled mineralogical composition of system following equilibrium titration of 100 kg of Hutton Sandstone (848.2m) to 10 kg of high-salinity and low-salinity formation waters at 60°C and a fixed $p\text{CO}_2 = 10^{-1.5}$ bar. Mineral mass given in kg.

	Initial	Saline	Low-Salinity
Quartz	38.25	37.65	37.66
Albite	12.95	13.03	12.87
K-Feldspar	5.80	11.46	11.46
Illite	13.02	0	0
Kaolinite	22.33	32.7	32.52
Chlorite	3.59	0	0
Calcite	0.45	0	0
Pyrolusite	0.01	0	0
Pyrite	0.04	0.04	0.04
Hematite	1.28	1.30	1.29
Magnesite	0	0.34	0.34
Dolomite	0	0.84	0.83
Siderite	0	2.41	2.41

Simulations suggest disequilibrium will drive geochemical reactions between formation waters and the Hutton Sandstone under ambient conditions, with the eventual dissolution of various silicate and carbonate minerals and the precipitation of clays. The presence of the reactive minerals under pre-injection conditions suggests kinetic controls on mineral dissolution are regulating formation water composition in the Hutton Sandstone.

Sequestration conditions

To generate a first-pass assessment of the potential CO_2 -water-rock interaction under sequestration conditions in the Surat Basin, GWB was used to model equilibrium reactions between the formation mineralogy and CO_2 -saturated groundwater. In the sequestration models closed boundary conditions for CO_2 are assumed, replicating the consumption of $\text{CO}_2(\text{aq})$ as dissolved gas is consumed by geochemical reactions within the formation.

Figure 14 illustrates a gradual water-rock- CO_2 equilibrium between Precipice Formation mineralogy and CO_2 -enriched high-salinity formation water at 60°C and 80 bar. The low salinity of formation waters and the limited quantity of reactive minerals precludes any significant buffering of formation water pH. It also limits the release of cations, leaving formation waters undersaturated for all carbonate minerals except siderite.

Under storage conditions the Hutton Sandstone, with a higher soluble mineral content, is more reactive than the Precipice Sandstone. Following addition of CO_2 -saturated water, model results indicate that dissolution of chlorite, calcite, and illite would occur, as observed in the baseline model. The acidic formation waters also enhance dissolution of albite and hematite. Mineral dissolution has a buffering effect on pH and releases cations into solution leading to more carbonate precipitation than in the Precipice Sandstone.

Figure 15 illustrates the change in carbonate saturation and pH as CO_2 -charged saline formation water reacts with Hutton Sandstone. Following CO_2 injection, saturation is rapidly reached for several carbonate minerals with dolomite and siderite precipitating in the largest quantities. Despite saturation being reached, the absolute quantities of precipitate potentially formed in the Hutton Sandstone are limited by the low formation TDS and low quantities of reactive minerals.

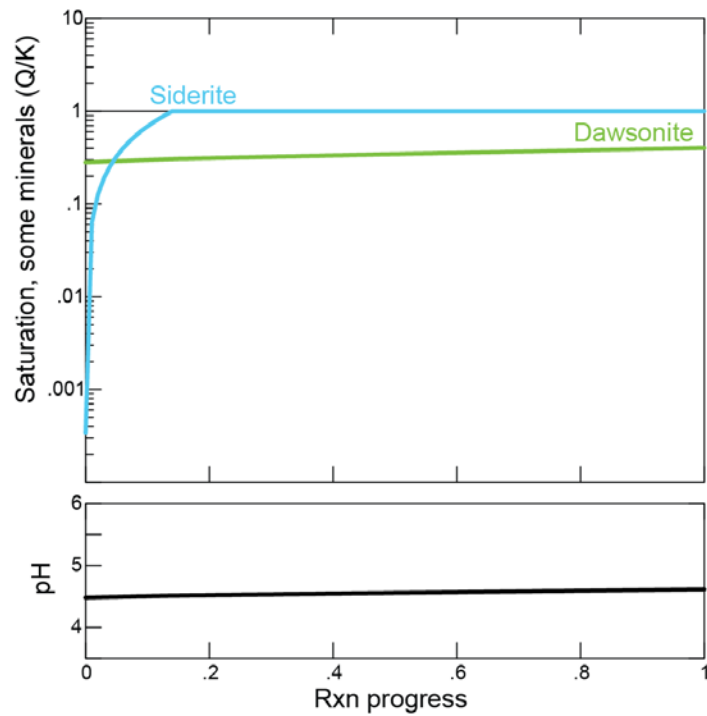


Figure 14: Change in carbonate saturation during Precipice Sandstone reaction with CO₂ saturated high salinity (TDS= 3356 mg/L) formation water at 60°C and 80 Bar.

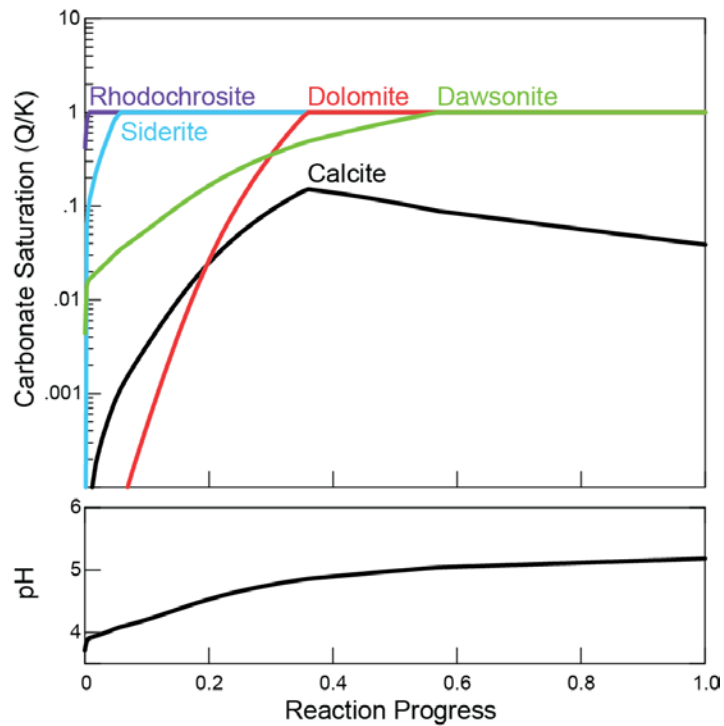


Figure 15: Change in carbonate saturation during Hutton Sandstone reaction with CO₂ saturated high salinity (TDS= 3013 mg/L) formation water at 60°C and 80 Bar.

Given that many of the divalent cations (e.g. Ca²⁺, Mg²⁺) in the Hutton Sandstone are contained in highly soluble minerals such as calcite, while Na⁺ is contained in less-soluble feldspars, dissolution kinetics will determine the sequence of carbonate precipitation during CO₂ sequestration in the Hutton Sandstone.

3.4. Discussion

Groundwater in the Surat Basin is fresher than in many geosequestration reservoirs elsewhere. The low salinities and temperatures in the prospective reservoirs are favourable for solubility trapping of carbon dioxide, with a maximum CO_2 solubility of 200-220 mol CO_2/m^3 assuming a 20% effective porosity. However, several hydrodynamic factors inhibit formation waters from reaching the maximum $\text{CO}_2(\text{aq})$ concentration, and concentrations in the storage reservoir are likely to be less than the maximum solubility limit.

Mineral trapping is not expected to be a significant sink for CO_2 in the mature Precipice Sandstone. The limited reactivity of the reservoir matrix and the low solute content of formation waters preclude the precipitation of significant quantities of carbonate minerals during CO_2 sequestration.

Conditions in the Hutton Sandstone may be more favourable for mineral trapping, but still quite low. Equilibrium modelling suggests that carbonate minerals siderite and dolomite could form under natural formation conditions. Equilibrium models also suggest dawsonite may form as a result of albite dissolution; however, kinetic controls on feldspar weathering will likely limit the availability of Na^+ and Al^{3+} in solution necessary for dawsonite precipitation.

Given the apparent kinetic controls on mineral dissolution and carbonate precipitation in the Surat Basin, reaction path models integrating reaction kinetics are needed to more accurately constrain the mineral trapping capacity of the Hutton and Precipice Sandstones. Development of such models and their application to co-contaminant studies are detailed following section.

4. Modelling the reactive transport of CO₂ and co-contaminants

Reactive transport models (RTM) provide the ability to generate predictions as to the physical and chemical evolution of the scCO₂-water-rock systems that are the result of carbon/carbon-co-contaminant storage. In order to construct reactive transport models, evaluation of the geochemical system through reaction path geochemical modelling allows for greater insight as to the constraints that can be applied thereby reducing the computational requirements of the RTM. A quantitative analysis of the mineral phases present in the formation of interest is required and, through reaction path modelling, the potential product mineral phases can be determined. Numerical modelling allows for the testing of the sensitivity of the model outcome to the input parameters and the identification of key parameters that must be determined to ensure the simulations are valid. This is particularly important when studying the co-contaminant SO₂ because it has a much higher solubility than most other co-contaminants of coal combustion and it can form a strong acid upon dissolution in the aqueous phase ($3\text{SO}_2 + 2\text{H}_2\text{O} \rightarrow 2\text{H}_2\text{SO}_4 + \text{S}$). Understanding how the rock units of a potential storage site will behave under acidic conditions associated with co-contaminant storage is a vital part of site evaluation. Here, reaction path geochemical modelling and reactive transport modelling play an important role.

4.1. Geochemical modelling

The geochemical modelling consists of 3 parts: (1) equilibrium modelling, (2) kinetics based reaction path modelling and (3) reactive transport modelling. Equilibrium modelling is used to evaluate the quality of the water analyses and to correct analytical values (or estimate missing analytical values) by assuming equilibrium between the formation minerals and the water at the temperature of interest. This gives the starting formation water composition for the remaining geochemical modelling. Kinetics based reaction path modelling involves combining the mineral phases and the aqueous and gas phases and allowing kinetically constrained reactions at the temperature and pressure of interest to proceed. It produces a detailed evaluation of the potential reactions which can occur as a function of time. A 'batch' reaction path model predicts the changes in rock and water composition over time following the initial mixing of a given rock with CO₂-saturated formation water. In reactive transport modelling, the system is both dynamic and open in that it involves the flow and transport of the aqueous and non-miscible phases through a porous medium made up of the mineral phases. It produces a spatial and temporal map of the potential reactions which can occur.

The equilibrium modelling was undertaken using the Spec8 and React modules of Geochemist's Workbench™ software package (Bethke and Yeakel, 2012) with a modified EQ3/EQ6 thermodynamic database (Delany and Lundeen, 1989). The reaction path modelling was undertaken using the React module of the Geochemist's Workbench™ software package (Bethke and Yeakel, 2012). The reactive transport modelling was undertaken using the TOUGHREACT program of Lawrence Berkeley National Laboratories (Xu et al., 2012).

Computer modelling of geochemical reactions requires the use of well-defined stoichiometric mineral phases for which thermodynamic data and kinetic rate data is available. The thermodynamic database for mineral and aqueous species used is based on the EQ3/6 database (Delany and Lundeen, 1989). Thermodynamic data for chlorite (Fe:Mg 3:1) and ankerite (Ca:Fe:Mg 1:0.5:0.5 and 0.6:0.35:0.15) were calculated using the methods by Holland (1989) and Vieillard (2002). For non-stoichiometric minerals, thermodynamic data can be calculated if the specific composition is known, but for minerals like smectite and illite, the compositional variability makes the use of end-members more viable. Smectite and illite were assigned a specific composition based on an idealised chemical structure.

The geochemical modelling involved the use of kinetic rate data to simulate changes in composition with time. This technique provides for equilibrium between mineral and fluid composition to be achieved by dissolving under-saturated or precipitating super-saturated phases at rates defined in the kinetic rate data input. The mineral phases used in the simulations are user defined. The phases initially present in the system are those described for each formation at a mass in correct proportion to the water:rock ratio calculated for 1 kg water using the measured porosity.

The reaction rate equation is the product of the mineral reactive surface area, a reaction rate constant specific to that mineral and the proximity to equilibrium between the mineral and the solution as shown in Eq. 7 (Lasaga, 1995).

$$r_k = A_s k_+ \left(1 - \frac{Q}{K}\right) \quad (7)$$

r_k = reaction rate

A_s = mineral surface area

k_+ = rate constant

Q = activity product

K = equilibrium constant

A more complex form of Eq. 7 is used when the effects of an inhibiting or catalysing species has to be taken into account.

$$r_k = A_s k_+ \prod_j (a_j)^{P_j} \left(1 - \frac{Q}{K}\right) \quad (8)$$

a_j = activity of the catalysing or inhibiting species

P_j = power for species j

Typically the catalysing species are hydrogen ions and hydroxide ions, making the most common mechanisms studied those at acid, neutral and basic conditions. The full equation then becomes a sum of the acid, neutral and base reaction mechanisms.

Most rate constant data is reported at 25°C and must be extrapolated to higher temperatures using the Arrhenius equation and an estimate for the activation energy of the process. The pH dependent rate law used for mineral specific reaction rate scripts read by the React code is given by:

$$k = k_{25}^{nu} \left[\frac{-E_a^{nu}}{R} \left(\frac{1}{T} - \frac{1}{T_0} \right) \right] + k_{25}^H \left[\frac{-E_a^H}{R} \left(\frac{1}{T} - \frac{1}{T_0} \right) \right] a_H^{n_H} + k_{25}^{OH} \left[\frac{-E_a^{OH}}{R} \left(\frac{1}{T} - \frac{1}{T_0} \right) \right] a_H^{n_{OH}} \quad (9)$$

E_a =activation energy

R =molar gas constant

T_0 =reference temperature (298.15 K)

nu =neutral mechanism

H =acid mechanism

OH =base mechanism

a =activity of the catalysing species

n =power term

Rate constant, power dependence and activation energy data were taken from a number of sources. The data for quartz is from Rimstidt & Barnes (1980), for albite and K-feldspar, kaolinite, hematite and smectite from Palandri and Kharaka (2004) and data for calcite and dolomite from Plummer et al. (1978). Siderite and ankerite were set to that of siderite from Steefel (2001) and were assumed to have

similar rate constants and activation energies to those of dolomite at low pH. Illite data is from Köhler et al. (2003) and the chlorite data are based on Lawson et al. (2007).

The mineral surface area was determined based on average grain size for each mineral using the methods described in White (1995).

$$A_s = \frac{6}{\rho D} \lambda \quad (10)$$

ρ = mineral density (g/cm^3)

D = mineral grain diameter

λ = roughness factor (measured surface area / geometric surface area)

A roughness factor of 7 was used based on values reported in White (1995) for fresh surfaces and typical of grains of less than 100 μm in diameter. The reactive surface of a mineral is considered to be controlled by selective sites and are typically described as being between one and three orders of magnitude less than the surface roughness based surface area (Lasaga, 1995; White, 1995). Surface coating or armoring, grain to grain contacts, grain edge faces on minerals with a tabular morphology (including clays) and channelling of the reactive fluid flow all serve to limit the reactive surface area (Li et al., 2006; Sonnenthal et al., 2006; Zhu et al., 2006). To account for these effects, the model reactive surface areas used are derived by taking the calculated surface area from Eq. 10 decreased by a factor of 100, consistent with values described by Xu et al. (2006; 2010) for reactive transport modelling using TOUGHREACT. Zhu et al. (2006) report that grain coating of natural feldspars in the Navajo Sandstone resulted in the reduction of reaction rates on the order of 10^5 times that of laboratory determined rates.

Precipitation rates of mineral phases, especially alumino-silicate minerals are poorly constrained. Common practice is to use the dissolution rates with values assigned to the nucleation site density or an initial volume ratio relative to the volume of solids if the mineral is not present in the system. The reaction path modelling precipitation rates were generated based on modifications to the classical nucleation theory (Walton, 1967; Nielsen, 1983) and the non-linear portion of the Burton-Cabrera-Frank crystal growth theory (Burton et al., 1951) described by Pham et al. (2011) and Hellevang et al. (2013).

$$r_P = A_S k_P \left(\frac{Q}{K} - 1 \right)^2 - k_N \exp \left\{ -\Gamma \left(\frac{1}{(T_K)^{\frac{3}{2}} \ln \left(\frac{Q}{K} \right)} \right)^2 \right\} \quad (11)$$

k_P = precipitation rate constant

k_N = nucleation rate constant

Γ = pre-exponential factor for nucleation

The nucleation and precipitation rate equation was also written into the GWB React scripts described earlier.

4.2. Modelling results

The initial formation water compositions used in the GWB Spec8 program were those listed in Table 2. The Evergreen initial water compositions included a low salinity, a higher salinity Na-HCO₃ and a higher salinity Na-Cl-HCO₃ type. The water datasets were incomplete for the planned numerical modelling so missing data had to be calculated through equilibration with mineral phases present. In particular there was no aluminium and iron data or pH reported in the analyses. Similarly, dissolved silica data is subject to mineralogical controls and using values from outside of the study area can

lead to unlikely dissolution or precipitation scenarios. Poor quality water data is not necessarily a hindrance as the numerical models can generate values through the assumption of equilibrium with mineral phases present in the system. Missing data was generated by equilibrating the water with facies mineralogy. The dissolved silica content was modelled based on equilibrium with chalcedony rather than quartz. Chalcedony was used to set the silica content because detailed study of formation water from sedimentary basins suggest that quartz precipitation and thus quartz control on the silica content is insignificant below approximately 80°C (Bjorlykke and Egeberg, 1993). Equilibration was carried out at 60°C. Results for the final input water data are reported in Table 5.

Table 5: Equilibrated formation water composition in mg/kg.

SAMPLE ID	pH	HCO ₃ ⁻	Na ⁺	Ca ⁺⁺	K ⁺	Mg ⁺⁺	Al ⁺⁺⁺	Fe ⁺⁺	Cl ⁻	SiO ₂	SO ₄ ⁼
Hutton 1	8.2	300	190	1	1	1	1.8E-02	3.9E-04	120	37.8	1
Hutton 2	7.56	765	1000	8	5	1	4.7E-03	3.2E-02	1130	36.1	1
Precipice 1	6.68	389	55	68	10	30	6.3E-04	1.5E+00	115	35.4	15
Precipice 2	7.62	2249	860	2.1	4.3	9.9	5.4E-03	1.0E-02	87	36.2	2

Geochemical reaction path modelling was conducted for each of the core samples from the Chinchilla 4 (35) and Roma 8 (16) cores for a total of 51 samples. The initial simulations were run with only the addition of CO₂ and subsequent simulations were run with CO₂ and SO₂ for each water type resulting in 274 simulations. The models are static with the initial CO₂ content set at 1.12 molar and for the CO₂ and SO₂ models, the SO₂ content was set at 0.18 molar. Simulations were run for 100 years total time. The following section reports on the samples listed in Table 3.

Conceptually the models can be understood as simulating what happens when CO₂ saturated (from P, T, composition) water comes in contact with the formation mineralogy. The amount of CO₂ available is only what is dissolved in the water so it can be likened to a part of the reservoir/seal that is not in direct contact with the supercritical phase. The simulations give an indication of how reactive the rocks are and their capacity to buffer the pH for the given conditions. Additional simulations will be run where the supercritical fluid pressure will be held constant, enabling the evaluation of the total capacity of the rocks to buffer pH. These models can be thought of as representing parts of the reservoir and seal that are in contact with the CO₂-saturated water either proximal to the plume or in contact with residual supercritical fluid trapped in the pore space.

4.2.1. Precipice Sandstone

The Precipice Sandstone sample 1190 contains low amounts of reactive mineral phases and thus shows only minor reactivity (Figures 16, 17). Only the phases that were reacting are included in the figures. Dissolving phases include chlorite, albite and to a minor degree illite while precipitation of kaolinite, chalcedony and siderite are simulated.

Initially, siderite dissolution takes place in the low salinity water simulation until equilibrium between siderite and the water occurs. During this time, chlorite dissolution also occurs, releasing iron into solution, this eventually leads to saturation then supersaturation of siderite and subsequent precipitation. In the simulation using higher salinity formation water, there is a much smaller initial siderite dissolution period before precipitation is initiated. Overall there is slightly higher dissolution and precipitation in the lower salinity formation water simulation. The difference between the two simulations can be attributed to the higher initial bicarbonate content contributing to pH buffering and thus a higher initial pH at higher salinity.

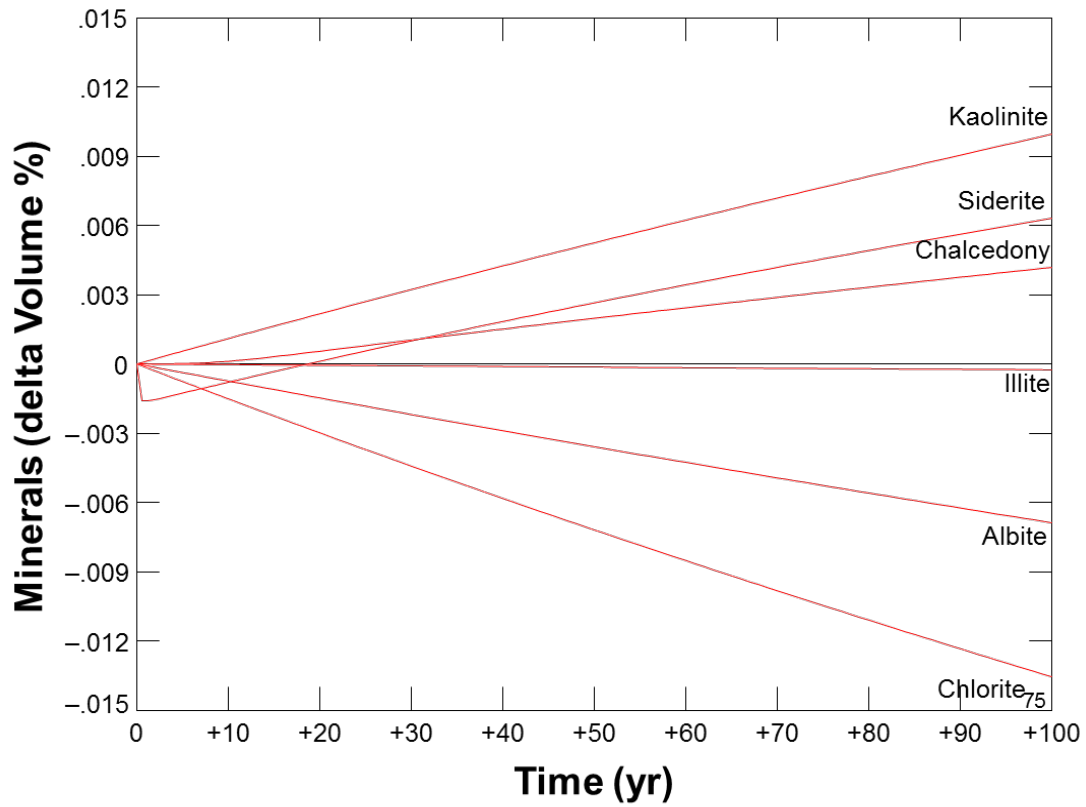


Figure 16: Reaction path modelling outcome for the Precipice Sandstone sample 1190 using the low salinity Precipice formation water.

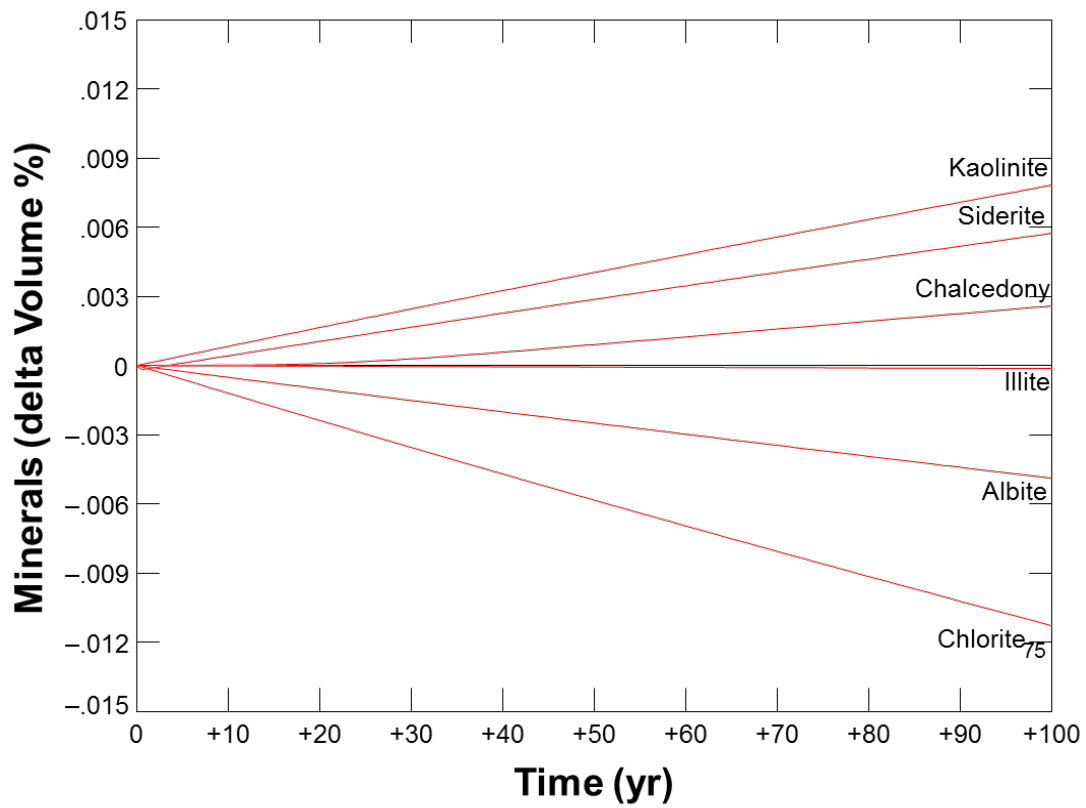


Figure 17: Reaction path modelling outcome for the Precipice Sandstone sample 1190 using the higher salinity Precipice formation water with CO₂ only.

The total amount of chlorite dissolution in 100 years is approximately 10% of the initial chlorite present. The initial weight % chlorite (assigned through LPNORM analysis) is lower than the detection limits of the XRD and only detectable through SEM, thus the uncertainty on this value is critical for determining the availability of reactive chlorite. Running the same simulation without any initial carbonate minerals produces a very slightly higher amount of siderite precipitation compared to the simulations with carbonate which suggests that the system is not very sensitive to the presences of carbonate minerals.

The simulation that included the co-contaminant SO₂ is shown in Figure 18. The amounts of minerals reacted increases at least 3-fold. In contrast to the pure CO₂ simulations, all of the siderite is dissolved and no carbonate precipitation occurs. Pyrite precipitation is predicted based on the SO₂ disproportionation reaction producing sulphuric acid and hydrogen sulphide. The sulphuric acid drives the siderite dissolution and the iron and sulphide precipitate as pyrite thus the reactions mirror each other on the reaction trace. The model shows the initial dissolution of kaolinite in the low pH solution (pH 1.5) however, the dissolution of chlorite and albite result in kaolinite saturation and precipitation after approximately 40 years. After 100 years the pH remains below 2.7 with very little buffering due to the low reactive mineral content. Simulations run without the presence of carbonate show very similar amounts of total dissolved and precipitated and that while carbonates are important, they are not controlling factors in these rocks. The simulations of CO₂ with co-contaminant SO₂ suggest that the Precipice has low reactivity, which was concluded from reaction path modelling involving CO₂ only (Section 3.3) as well. Consequently, mineral trapping is expected to play a minor role.

4.2.2. Hutton Sandstone

There is little difference between the simulations using the 2 formation water compositions (Figures 19, 20). The lower salinity water shows a slightly higher amount of albite dissolution likely reflecting a greater degree of undersaturation of the fluid with respect to albite upon introduction of the CO₂. The Hutton Sandstone does contain a higher proportion of reactive mineral phases than the Precipice Sandstone and that is reflected in the extent of reaction in the 100 years of simulated time. The individual mineral amounts show up to 0.25 volume % change. Similar to the previous simulations, chlorite and albite are the most reactive phases. Calcite dissolution also occurs but following the initial reaction, a period of precipitation is predicted until dolomite supersaturation and precipitation occurs, after which dissolution of calcite continues. Kaolinite, siderite, dolomite and chalcedony are the precipitating phases.

The mineralogy of the Hutton Sandstone suggests that there is significant reactivity with relatively high chlorite and albite. The extent of reaction indicated by the simulations suggests that the Hutton Sandstone provides a reasonable pH buffering capacity and divalent metals to drive CO₂ trapping by mineral precipitation.

The presence of SO₂ results in more extensive calcite dissolution and the precipitation of anhydrite and pyrite but produces few other changes in the simulation (Figure 21). Calcite reacts quickly forming dissolved carbonate species which buffer the pH above 4. The pH at the end of the simulation is just slightly lower than the simulation with CO₂ only. These model outputs indicate that the presence of small amounts of carbonate in rocks can play a significant role in neutralizing the effects of SO₂ disproportionation and oxidation reactions that generate sulphuric acid.

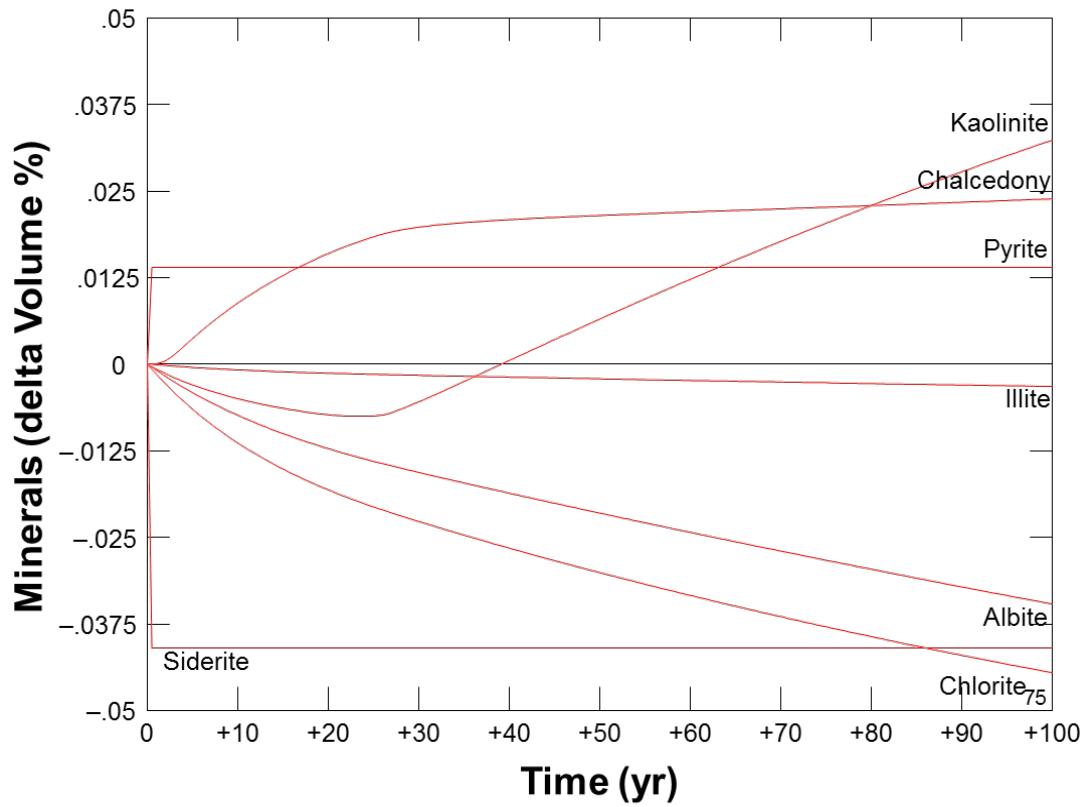


Figure 18: Reaction path modelling outcome for the Precipice Sandstone sample 1190 using the higher salinity Precipice 2 formation water with CO₂ and SO₂.

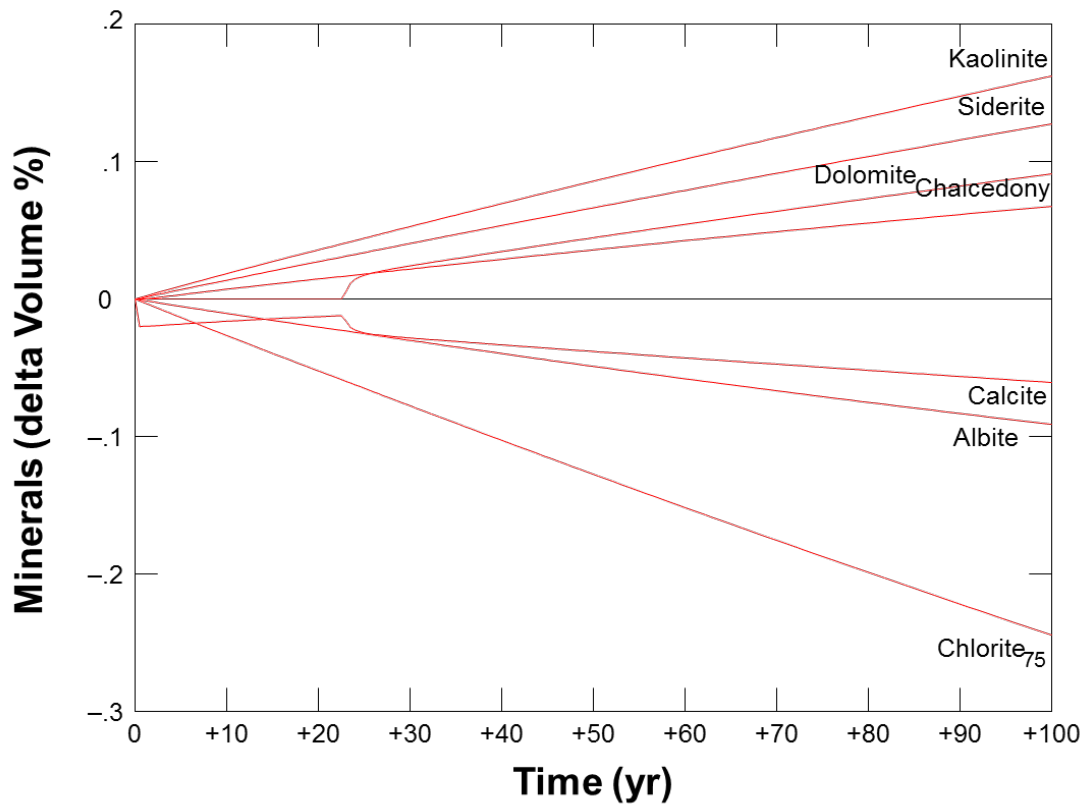


Figure 19: Reaction path modelling outcome for the Hutton Formation sample 848 using the lower salinity Hutton 1 formation water composition.

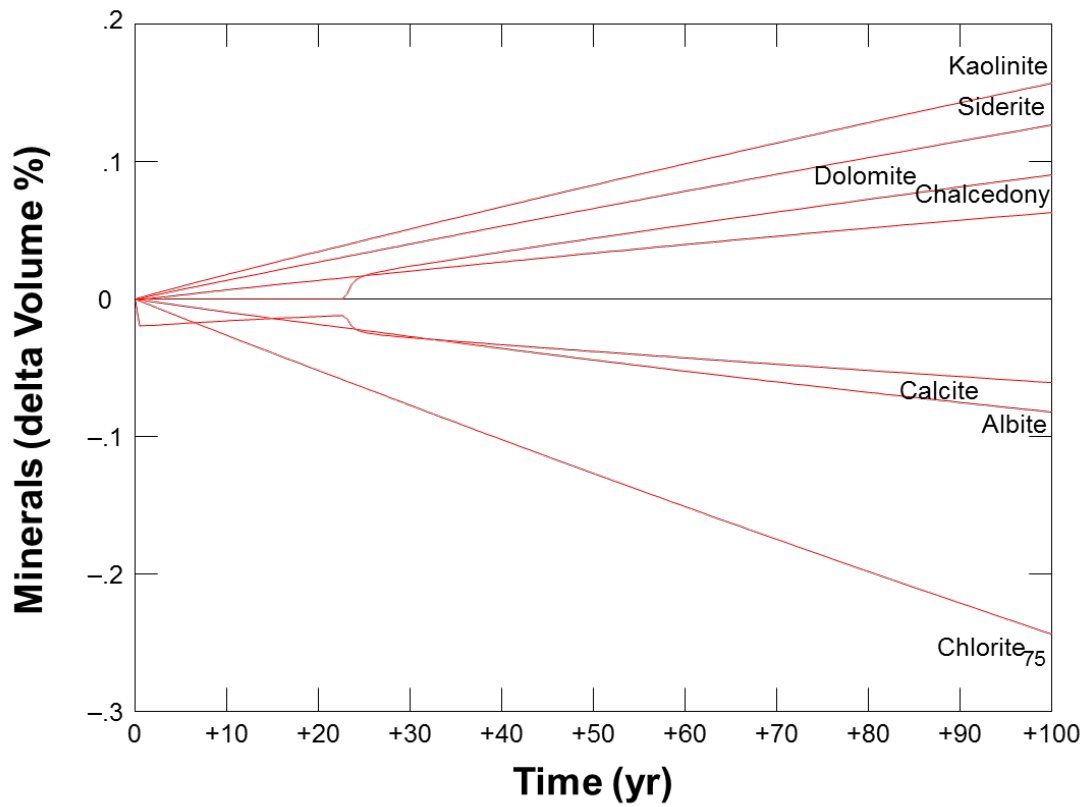


Figure 20: Reaction path modelling outcome for the Hutton Formation sample 848 using the higher salinity Hutton 2 formation water composition.

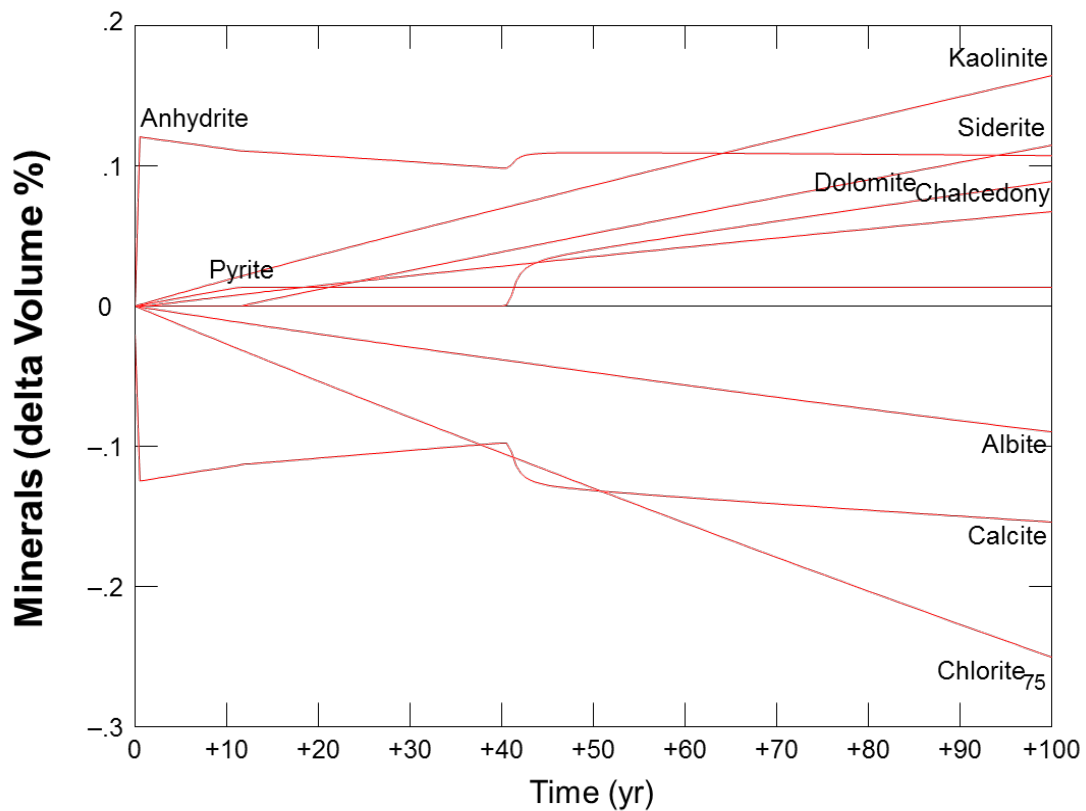


Figure 21: Reaction path modelling outcome for the Hutton Formation sample 848 using the higher salinity Hutton 2 formation water composition with CO₂ and co-contaminant SO₂.

4.3. Discussion

The reaction path modelling has provided a number of insights into the chemistry of the Surat Basin system and highlights a number of factors that require attention. Chemically the rocks of the Precipice and Hutton sandstones have some similarities that show up in reaction path simulations as the same reacting minerals and reaction mechanisms. This is not a surprise as they represent an evolving depositional environment but not a significant change in provenance of the sediments. The modelling indicates that particular attention has to be paid to qualifying and quantifying the reactive mineral phases in these rocks (e.g. albite, chlorite, and carbonates). This needs to be integrated with the bulk chemistry to ensure that the minerals are well characterised chemically. Methods like thin section petrological examination and SEM with EDS are particularly useful but new techniques like Hylogger and QEMSCAN provide additional information. Inconsistencies regarding the mineralogy still need to be resolved and the integration of Hylogger and QEMSCAN with the continuous data along the length of the core may present opportunities to generate clustered assemblages of like behaving mineralogies.

The use of scripts written for the GWB React module has proven a significant improvement over the built in rate law capabilities. In particular, the new scripts calculate the rate at variable pH based on the extended rate equation while the built in rate law does not allow this. Also, by incorporating nucleation and crystal growth equations into the precipitation mechanisms, it is believed a more accurate model is produced. A good example is the predicted precipitation of dawsonite based on thermodynamic data, but an appropriate kinetic model would inhibit precipitation.

The reactive transport modelling will be, in part, accomplished using TOUGHREACT (Xu et al., 2012). This software allows coupled multiphase fluid and heat flow, solute transport and chemical reactions. At this point in time, TOUGHREACT does not have the capability to include co-contaminants. However, a new Equation of State, EOS, accounting for the major co-contaminants SO_x, NO_x and O₂ has recently been developed (Ziabakhsh-Ganji and Kooi, 2012) and a beta version of its implementation in TOUGHREACT will be tested and modified to enable CO₂ plus co-contaminant reactive transport. The software code STOMP was purchased and it includes a module that enables reactive transport with co-contaminants. This code will also be utilized in the study. The initial model is being set up as a 2D grid that incorporates the physical and chemical heterogeneity of the Precipice Sandstone to Evergreen Formation sequence defined in core GSQ Chinchilla 4.

5. The regional stress field and implications for fault stability

5.1. Introduction

A key component for developing fault stability models is a moderate to good understanding of the in situ stress field in the vicinity of the faults of interest. Unfortunately, there is currently very limited stress information on the Surat Basin. According to the Australasian Stress Map (ASM) database (Figure 22, <http://www.asprg.adelaide.edu.au/asm/>), which is the most comprehensive database available, only 3 measurements characterising the horizontal stress direction exist, although more stress orientation information is available for the Bowen Basin to the north. It is therefore crucial that some additional information is added to this database in order to determine faulting mode, stress due to the overburden, and minimum horizontal stress magnitude. Without some clarity on these parameters, it is very difficult or impossible to assess fault stability under a CO₂ injection scenario.

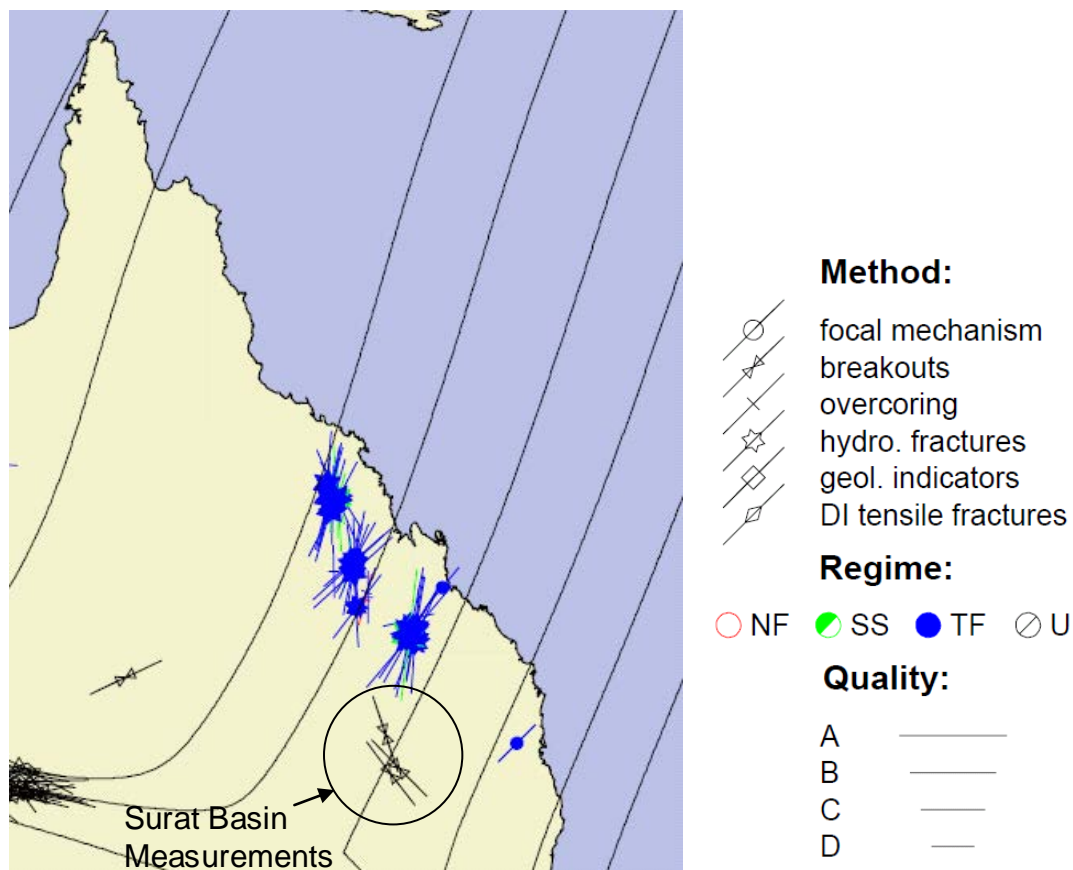


Figure 22: Horizontal stress measurements currently available for eastern Queensland (<http://www.asprg.adelaide.edu.au/asm/>). Arrows show the orientation of the maximum horizontal stress. NF: Normal Fault, SS: Strike-Slip Fault, TF: Transverse Fault, U: Undetermined. Note, how limited information is available for the Surat Basin.

Various well data and recent data from publications were examined in order to gain a first pass understanding of Surat Basin geomechanics. The results of this analysis, presented here, will help constrain the geomechanical response under various modelled CO₂ injection scenarios. In such a first pass geomechanical study, the first priority is to gain an understanding of the in situ stress field, which

comprises the orientations of the two horizontal stresses and the magnitudes of the three principal stresses. The orientations of the horizontal stresses are generally acquired by image log interpretation, by measuring the orientations of borehole breakouts and drilling induced tensile fractures. The magnitude of the vertical stress is calculated mainly by integrating density logs, with check shot data or sonic logs used to fill in any gaps that exist. Leak off tests are generally used to determine the magnitude of the minimum horizontal stress. The magnitude of the maximum horizontal stress is generally the hardest to determine, especially if no rock mechanical data is available. Frictional limit theory is generally used to determine the upper bound for the maximum horizontal stress and is used here (Moos and Zoback, 1990; Sibson, 1974).

5.2. New data

A significant amount of new stress orientation data was either newly interpreted or found in recent publications. The Queensland government provided significant well data, some of which contained image log data that could be analysed for the presence of borehole breakouts and drilling induced tensile fractures. Five of the wells containing image logs possessed such features that could be interpreted for stress orientation information. Four of the five wells are from the northern portion of the Surat Basin, and one was located in the south (see Figure 23). The other important source of new stress orientation information was provided by the work of Brooke-Barnett et al. (2012). This work was presented (but unpublished), and we thank Brooke-Barnett and Origin Energy for providing detailed information regarding well locations and image log interpretations. The locations of the wells are shown in Figure 23 and Table 6. Stress orientations for two other wells were also provided from studies by Khaksar et al. (2012) and Johnson et al (2010).

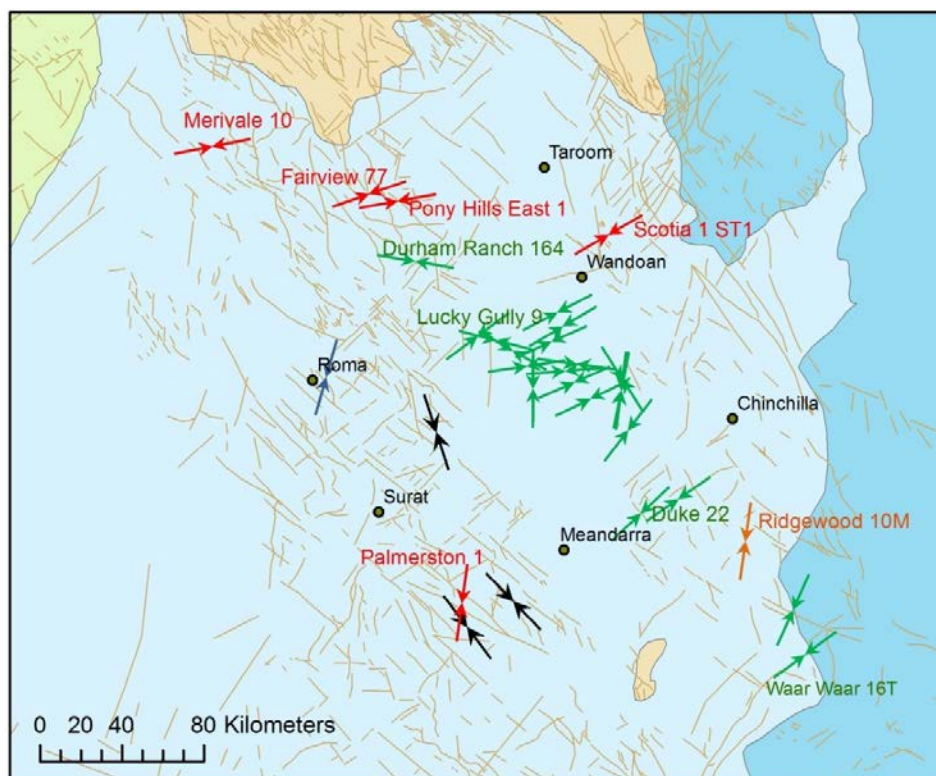


Figure 23: New stress orientation information available for the Surat Basin, as interpreted from borehole breakouts and drilling induced tensile fractures in wells. Arrows indicate the orientation of the maximum horizontal stress. Red arrows: new stress data interpreted in this study, Green arrows: stress data provided by Brooke-Barnett et al (2012), Blue arrow: unknown Roma well of Khaksar et al. (2012), Orange arrow: from Johnson et al. (2010), Black arrows: previous available stress data from the Australasian Stress Map Database.

Table 6: Surat wells containing image logs that provide information on the orientation of the maximum horizontal stress. FMI: Fullbore formation micro-imager, UBI: Ultrasonic borehole imager, CMI: Compact micro-imager.

Well Name	Latitude	Longitude	Log Type	Max Stress Orient. (°)	Reference
Carinya 7	-26.544	149.885	FMI	86	Brooke-Barnett et al. (2012)
Carinya 8	-26.512	149.937	CMI	98	Brooke-Barnett et al. (2012)
Carinya South 2	-26.669	150.001	FMI	64	Brooke-Barnett et al. (2012)
Condabri MB9H	-26.808	150.171	CMI	38	Brooke-Barnett et al. (2012)
Dalwogan 12	-26.631	150.146	FMI	11	Brooke-Barnett et al. (2012)
Dalwogan 14	-26.631	150.146	FMI	8	Brooke-Barnett et al. (2012)
Dalwogan 16	-26.630	150.146	FMI	7	Brooke-Barnett et al. (2012)
Dalwogan 9	-26.571	150.135	FMI	148	Brooke-Barnett et al. (2012)
Duke 14	-27.174	150.224	FMI	47	Brooke-Barnett et al. (2012)
Duke 22	-27.111	150.389	FMI	55	Brooke-Barnett et al. (2012)
Durham Ranch 164	-26.061	149.226	FMI	100	Brooke-Barnett et al. (2012)
Fairview 77	-25.769	149.027	FMI	71	New Interp, this study
Gilbert Gully 18	-27.598	150.898	FMI	24	Brooke-Barnett et al. (2012)
Horse Creek 16	-26.449	149.652	FMI	120	Brooke-Barnett et al. (2012)
Lucky Gully 11	-26.394	149.508	UBI	53	Brooke-Barnett et al. (2012)
Lucky Gully 9	-26.407	149.582	FMI	105	Brooke-Barnett et al. (2012)
Merivale 10	-25.559	148.338	FMI	79	New Interp, this study
Noonga Creek 5	-26.523	149.717	FMI	82	Brooke-Barnett et al. (2012)
Palmerston 1	-27.565	149.448	FMI	8	New Interp, this study
Pony Hills East 1	-25.799	149.151	FMI	80	New Interp, this study
Ramyard 15	-26.418	149.829	FMI	66	Brooke-Barnett et al. (2012)
Ridgewood 10M	-27.294	150.691		8	Johnson et al. (2010)
Roma 1	-26.575	148.850		16	Khaksar et al. (2012)
Scotia 1 ST1	-25.948	150.081	FMS	60	New Interp, this study
Talinga 31	-26.882	150.338	FMI	105	Brooke-Barnett et al. (2012)
Waar Waar 16T	-27.795	150.946	FMI	54	Brooke-Barnett et al. (2012)
Woleebee East 3	-26.289	149.856	FMI	63	Brooke-Barnett et al. (2012)
Woleebee East 5	-26.352	149.880	FMI	59	Brooke-Barnett et al. (2012)
Wygi Creek 2	-26.623	149.761	UBI	0	Brooke-Barnett et al. (2012)
Wygi Creek 3	-26.597	149.929	UBI	66	Brooke-Barnett et al. (2012)

5.3. Results and discussion

The new orientation data acquired in this study is particularly valuable for two reasons. Firstly, it fills a large gap that previously existed for Queensland and Australia in general. Secondly, when one looks at all the new data in Figure 23, one notices that there is significant variability in the stress orientations, with most new measurements being significantly different than the few currently available in the Australasian Stress Map Database. Based on Figure 23 it appears that the maximum horizontal stress is roughly E-W in the northern and central-eastern portions of the basin. In the southern and western portions of the basin the stress orientation rotates toward a more N-S orientation. However, there is significant variability in the data, the origin of which is not understood. One can see that the stress orientations of the Surat Basin are far more complex and variable than the orientations in the Bowen Basin to the north (Figure 23).

Determining the magnitudes of the three principal stresses is of great importance when characterising fault stability or the pressure at which tensile fracturing of the formation will take place. The relative magnitudes of the three principal stresses determine whether faulting will be in a normal, strike-slip or thrust mode. Due to the paucity of published geomechanical information on the Surat Basin, the predominant faulting mode is not constrained. However, newly interpreted data from this study and several recent publications (Brooke-Barnett et al., 2012; Khaksar et al., 2012; Johnson et al., 2010) focussed on different parts of the Surat Basin provide much needed, consistent information regarding the magnitudes of the 3 principal stresses in the Surat Basin.

In nearly all geomechanical treatments, the in situ stress field is assumed to be Andersonian (Anderson 1951), in which one of the three principal stress axes is oriented vertically. In such a case, the magnitude of the vertical stress is equivalent to the weight of the overburden. To determine the stress driven by the overburden, one can use density logs from a vertical well and integrate the density logs over depth to determine the vertical stress gradient. We have done this here for 4 of the newly interpreted wells in the Surat Basin. The results of the vertical stress calculation are shown in Figure 24. All four wells are roughly in agreement with each other and indicate a vertical stress gradient of 20-22 MPa/km over the interval 0-2000 m.

When these newly calculated values for the vertical stress gradient are compared to the three recent geomechanical studies on the Surat Basin (Brooke-Barnett 2012; Johnson et al. 2010; Khaksar et al. 2012), we find a very high degree of consistency between our data and the 3 studies. For an unrevealed Roma well, Khaksar et al. find that the vertical stress gradient is 22 MPa/km. For the Ridgewood 5 and Ridgewood 10M wells, Johnson et al. have determined that the vertical stress is also 22 MPa/km. Finally, Brooke-Barnett et al. have determined that the vertical stress lies in the range 20-22 MPa/km, as we have in this study.

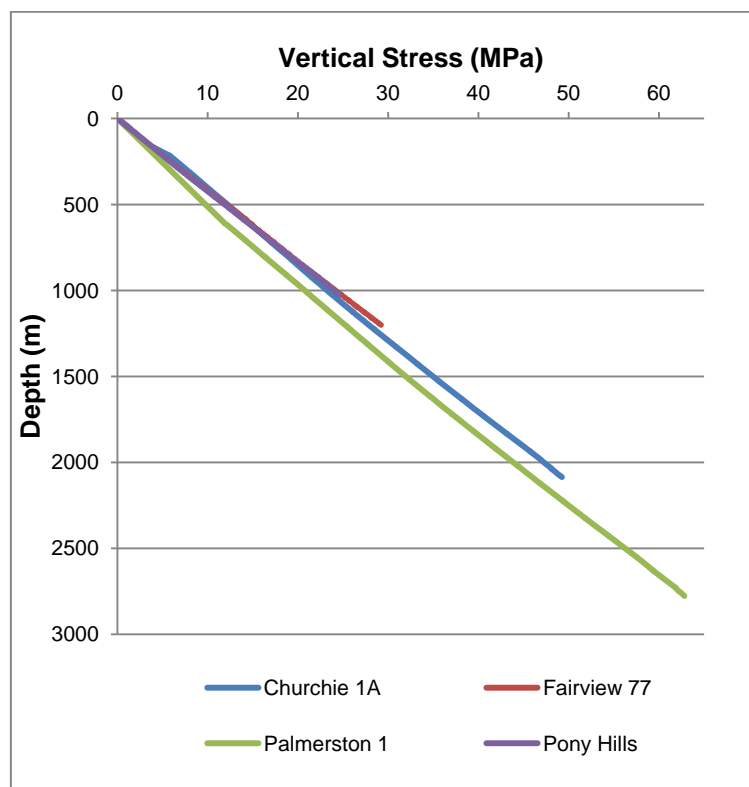


Figure 24: Vertical stress profile for four wells acquired by integrating density logs over depth. Results are consistent with each other and suggest that the vertical stress magnitude is between 20-22 MPa km⁻¹.

A number of well completion reports were provided by the Queensland Government for examination. It was hoped that these reports would contain leak off test or formation integrity tests that could be used for determination of the minimum horizontal stress magnitude. However, unfortunately nearly none of the well completion reports examined contain this information. Either the information was not included or the tests were not conducted. We therefore use detailed leak off test and fracture test data provided in publications to constrain this value. The results of these detailed tests are shown in Table 7.

It is evident, from Table 7, that there is great consistency across the Surat Basin for the minimum horizontal stress magnitude. Based on the results of these studies, we herein use a value of 20 MPa km⁻¹ as the estimate for the minimum horizontal stress magnitude.

Table 7: Minimum horizontal stress values acquired at various wells in the Surat Basin.


Well Name	Technique	Min Horiz Stress (MPa/km)	Reference
P-1 (unknown Roma well)	LOT's, CSFT	21	Khaksar et al. (2012)
P-2 (unknown Roma well)	LOT's, CSFT	22	Khaksar et al. (2012)
Ridgewood 5	Frac tests	18	Johnson et al. (2010)
Ridgewood 10M	Frac tests	19	Johnson et al. (2010)
Durham Ranch 164	LOT/mini-frac	19	Brooke-Barnett et al. (2012)
Lucky Gully 19	LOT/mini-frac	15	Brooke-Barnett et al. (2012)
Duke 22	LOT/mini-frac	19	Brooke-Barnett et al. (2012)

The magnitude of the maximum horizontal stress is generally the hardest component of the stress tensor to determine, especially in the absence of rock mechanical test data. Rock mechanical tests can be used in conjunction with the observation of borehole breakouts to infer the stress that caused the wellbore to fail. Khaksar et al. (2012) use this to infer that the maximum horizontal stress in the Roma area under normally pressured conditions is about 26 MPa km⁻¹. For the Ridgewood wells, Johnson et al. (2010) found the maximum horizontal stress magnitude to be 27-32 MPa km⁻¹. Finally, Brooke-Barnett (2012) find the maximum horizontal stresses to be more variable between wells and also with depth, ranging from about 20 MPa km⁻¹ to 38 MPa km⁻¹. It should be noted that many of the wells have decreasing stress gradient with depth, with the faulting mode going from strike-slip to a borderline strike-slip to normal mode, in which the vertical stress becomes equal to the maximum horizontal stress.

Frictional limit theory can also be used to estimate the maximum value for the maximum horizontal stress. Frictional limits theory states that the ratio of the maximum to minimum effective stress cannot exceed the magnitude required to cause faulting on an optimally oriented, pre-existing, cohesionless fault plane (Sibson 1974). The frictional limit to stress is given by

$$\frac{S_1 - P_p}{S_3 - P_p} \leq \left(\sqrt{(\mu^2 + 1)} + \mu \right)^2 \quad (12)$$

where μ is the coefficient of friction, P_p is the pore pressure, S_1 is the maximum principal stress and S_3 is the least principal stress. The maximum principal stress is assumed to be maximum horizontal stress. Assuming a friction coefficient of 0.6 and a minimum horizontal stress value of 20 MPa km⁻¹ in a hydrostatic regime, we find that S_1 (maximum horizontal stress) is 41.6 MP km⁻¹. This number places an upper bound on the value for S_1 , assuming the value for the coefficient of friction is correct.



The new data acquired for the Surat Basin has provided important new geomechanical information on the basin that will be crucial to future geomechanical studies. The most important contribution of this work are the numerous image log interpretations which provide significant coverage for the maximum horizontal stress orientation. In the northern part of the Surat Basin the maximum horizontal stress is approximately E-W, while further to the south and to the centre of the basin, the stress rotates to a more N-S direction.

When all the newly interpreted stress magnitude information is consolidated with the available published data, the stress regime in all parts of the Surat Basin appears to be a strike slip where the vertical stress is smaller than the maximum horizontal stress and larger than the minimum horizontal stress. However, the minimum horizontal stress and the vertical stress are usually quite similar, indicating a nearly hybrid strike-slip to thrust regime. In such a stress regime, faults with strikes that are approximately at 30 degrees to the maximum horizontal stress direction will be at greatest risk of reactivating due to them having highest shear to normal stress on the fault plane.

Due to the high degree of variability of stress orientations in the Surat Basin, it is recommended that any operational activities involving geomechanical risk be assessed individually, with specific emphasis on characterising the stress orientations. This report provides a first pass assessment of Surat Basin geomechanics, but clearly much more work is needed to characterise the stress tensor in detail, and understand the underlying factors that drive variability throughout the basin.

6. Conclusions

This interim report summarises geochemical and structural results relating to the project on fault stability and geochemical impacts under CO₂ storage conditions exemplified for the Surat Basin. Some results to date are conclusive, while other results clearly require further investigations as pointed out below.

A detailed lithostratigraphy has been derived for the cores GSQ Chinchilla 4 from the eastern flank and GSQ Roma 8 from the western flank of the Surat Basin. Core GSQ Chinchilla 4 serves as a reference core for this study due to its excellent cored rock record and its proximity to the EPQ7 tenement currently considered for CO₂ storage. Additional samples have been analysed from the two cores to extend the data base of petrographic, petrophysical, mineralogical and geochemical properties supporting the modelling of fluid-rock reactions and the coupled reactive transport of CO₂ together with co-contaminants (SO_x, NO_x, O₂). Additionally, the data base of horizontal stress data across the Surat Basin has been significantly extended by analysing image log data provided by the Queensland Government and by incorporating image log interpretations provided by Origin.

The prediction of the fluid trapping rate has utilised only analytical solutions to date. A very early onset of fluid density destabilisation and advective mixing is predicted particularly because of the high permeability (average of 1 darcy) of the Precipice Sandstone as a prospective reservoir. An analytical solution for the dynamic geometry of the CO₂ plume and the associated scCO₂-water interface in an isotropic reservoir has been applied, but this approach has been found insufficient. A numeric multi-phase transport model particularly accounting for vertical heterogeneity in the Precipice Sandstone, for example introduced by interbedded shales, is required for predicting a realistic fluid trapping rate.

Mineral dissolution and precipitation has been predicted for the Precipice and Hutton sandstones using representative Surat Basin formation water composition with an initial total dissolved solid concentrations in the range of 300 to 3000 mg L⁻¹. The Precipice Sandstone is a highly mature reservoir rock largely dominated by quartz and with significant amounts of kaolinite. It shows hardly any reactivity under CO₂ storage conditions. The Hutton Sandstone is mineralogically more variable and includes reactive minerals such as albite, K-feldspar and muscovite. Reaction path modelling suggests the precipitation of minor amounts of magnesite (Mg-carbonate) and large quantities of dawsonite (NaAl-carbonate). Dawsonite precipitation has been predicted and it has been critically discussed in several other studies before, because dawsonite is rarely observed in natural analogues. Therefore, these results are not trusted at this point and laboratory experiments will be undertaken to test the likelihood of dawsonite precipitation.

Reaction path modelling involving the co-contaminant SO₂ was carried out to evaluate the likely geochemical reactions relative to reactions involving CO₂ only. This is an essential step prior to reactive transport modelling (RTM) as it allows eliminating a large number of irrelevant reactions and thereby reduces RTM computation time significantly. Model results show higher reaction rates and a larger degree of mineral dissolution due to the formation of sulphuric acid through the disproportionation of SO₂. Further work is needed to characterise reactions involving reactive NO_x species. Secondly, anhydrite (CaSO₄) may form following the dissolution of calcite.

Stress orientation and magnitude data have been significantly enhanced for the Surat Basin through this study. The vertical stress lies consistently in the range of 20-22 MPa km⁻¹ and the minimum horizontal stress magnitude is estimated as 20 MPa km⁻¹. The maximum horizontal stress is generally the hardest to determine and it was found to be considerably variable between wells and with depth, ranging from about 20 to 38 MPa km⁻¹. The upper bound for the maximum horizontal stress is calculated as 41.6 MPa km⁻¹. In the northern part of the Surat Basin the maximum horizontal stress is approximately E-W, while further to the south and to the centre of the basin, the stress rotates to a more N-S direction. Based on the analysis to date, faults with strikes that are approximately at 30 degrees to the maximum horizontal stress direction will be at greatest risk of reactivating due to the highest shear to normal stress on the fault plane.

7. References

- Anderson EM, 1951, The Dynamics of Faulting and Dyke Formation with Applications to Britain. Edinburgh, Oliver and Boyd.
- Bethke CM, Yeakel S, 2012, The Geochemist's Workbench (Version 9.0): Reaction modeling guide. Aqueous Solutions, LLC, Champaign, Ill., 96 p.
- Bjorlykke, K. and Egeberg, P.K., 1993. Quartz cementation in sedimentary basins. *The AAPG Bulletin* 77: 1538-1548.
- Brooke-Barnett S, Flottmann T, Paul PK, Busetti S, Hennings P., Reid R, 2012, Influence of basement features on in situ stresses within the Bowen and Surat Basins, SE Queensland. APPEA CSG Conference and Exhibition, Brisbane, Australia, October, 8-10, 2012.
- Burton WK, Cabrera N, Frank FK, 1951. The growth of crystals and the equilibrium structure of their surfaces. *Phil. Trans. Royal Soc. London* 243: 299–358.
- Carbon Storage Taskforce, 2009, National Carbon Mapping and Infrastructure Plan – Australia: Concise Report, Department of Resources, Energy and Tourism, Canberra, 69pp.
- de Caritat P, Bloch J, Hutcheon I, 1994, LPNORM: A linear programming normative analysis code. *Comput. Geosci.* 20, 313-347.
- Coudrain-Ribstein A, Gouze P, De Marsily G., 1998, Temperature - carbon dioxide partial pressure trends in confined aquifers. *Chem. Geol.* 145: 73–89.
- Delany, J.M. and Lundeen, S.R., 1989. The LLNL thermodynamic database. Lawrence Livermore National Laboratory Report UCRL-21658.
- Duan Z. et al., 2006, An improved model for the calculation of CO₂ solubility in aqueous solutions containing Na⁺, K⁺, Ca²⁺, Mg²⁺, Cl⁻, and SO₄²⁻. *Mar. Chem.* 98: 131–139.
- Duan Z, Sun R, 2003, An improved model calculating CO₂ solubility in pure water and aqueous NaCl solutions from 273 to 533 K and from 0 to 2000 bar. *Chem. Geol.* 193: 253 – 271.
- Duan Z, Hu J, Di D, Mao S, 2008, Densities of the CO₂-H₂O and CO₂-H₂O-NaCl systems up to 647K and 100 MPa. *Energy Fuels* 22: 1666-1674.
- Ennis-King J, Patterson L, 2003, Role of convective mixing in the long-term storage of carbon dioxide in deep saline formations. SPE Annual Techn. Conf. Exhib. SPE 84344, Denver, Colorado.
- Farquhar SM et al., 2013, Mineralogical characterisation of a potential reservoir system for CO₂ sequestration in the Surat Basin. *Austr. J. Earth Sci.*, 60: 91–110.
- Gasda SE, Nordbotten JM, Celia MA, 2011, Vertically averaged approaches for CO₂ migration with solubility trapping. *Water Res. Research* 47, doi:10.1029/2010WR009075.
- Grigorescu M, 2011a, Mineralogy of the north-eastern Bowen Basin and north-eastern Surat Basin, Queensland. Queensland Geological Record 2011/02.
- Grigorescu M, 2011b, Jurassic groundwater hydrochemical types, Surat Basin, Queensland – a carbon geostorage perspective. Queensland Geological Record 2011/05.
- Haese RR, Frank AA, Grigorescu M, Horner K, Kirste D, McKillop M, Tenthorey E, 2013, Data and samples supporting the study of geochemical impacts and monitoring of CO₂ storage in low salinity aquifers. CO2CRC Report No RPT012-4019.
- Helgeson HC, 1969, Thermodynamics of hydrothermal systems at elevated temperatures and pressures. *Am. J. Sci.* 267: 729–804.
- Hellevang H., Pham V. T. H. and Aagaard P. (2013) Kinetic modelling of CO₂-water-rock interactions. *Int. J. Greenh. Gas Control* 15: 3-15.
- Herczeg AL, Torgensen T, Chivas AR, Habermehl MA, 1991, Geochemistry of groundwater from the Great Artesian Basin, *Austr. J. Hydrol.* 126: 225-245.
- Hodgkinson, J. & Grigorescu, M., 2012, Background research for selection of potential geostorage targets—case studies from the Surat Basin, Queensland. *Austr. J. Earth Sci.*:1–19.

- Hodgkinson J, Grogorescu M, Hortle A, McKillop M, Dixon O, Foster L, 2010, The potential impact of carbon dioxide injection on freshwater aquifers: the Surat and Eromanga Basins in Queensland. Queensland Minerals and Energy Reviews Series.
- Holland TJB, 1989. Dependence of entropy on volume for silicate and oxide minerals: a review and a predictive model. *Am. Mineralogist*, 74: 5-13.
- Johnson RL, Glassbrow B, Scott MP, Pallikathakathil ZJ, Datey A, Meyer J, 2010, Utilizing current technologies to understand permeability, stress azimuths and magnitudes and their impact on hydraulic fracturing success in a coal seam gas reservoir. *SPE Paper* 133066.
- Khaksar A., White A, Rahman K, Burgdorff K, Ollarves R, Dunmore S, 2012, Systematic geomechanical evaluation for short-term gas storage in depleted reservoirs. *APPEA Journal*, 129-148.
- Köhler SJ, Dufaud F, Oelkers EH, 2003, An experimental study of illite dissolution kinetics as a function of pH from 1.4 to 12.4 and temperature from 5 to 50°C. *Geochim. Cosmochim. Acta* 67: 3583-3594.
- Lasaga AC, 1995. Fundamental approaches in describing mineral dissolution and precipitation rates. In White AF and Brantley SL (Eds.), Chemical weathering rates of silicate minerals. Mineralogical Society of America, *Rev. Mineral.* 31: 23-86.
- Li L, Peters C A, Celia MA, 2006, Upscaling geochemical reaction rates using pore-scale network modeling. *Adv. Water Res.* 29, 1351-1370.
- Li D., Graupner BJ and Bauer S, 2011, A method for calculating the liquid density of the CO₂-H₂O-NaCl system under CO₂ storage condition. *Energy Procedia* 4: 3817-3824.
- Lowson RT, Brown PL, Comarmond M-J, Rajaratnam G, 2007, The kinetics of chlorite dissolution. *Geochim. Cosmochim. Acta* 71: 1431-1447.
- Moos D, Zoback MD, 1990, Utilization of observations of well bore failure to constrain the orientation and magnitude of crustal stresses: application to continental, Deep Sea Drilling Project, an Ocean Drilling Program Boreholes. *J. Geophys. Res.* 95: 9305-9325.
- Nielsen AE, 1983, Precipitates: formation, coprecipitation, and aging. IN Kolthoff IM, Elving PJ (Eds.), *Treatise on Analytical Chemistry*, Wiley (1983), pp. 269–347.
- Neufeld JA, Hesse MA, Riaz A, Hallworth MA, Tchelepi HA, Huppert HE, 2010, Convective dissolution of carbon dioxide in saline aquifers. *Geophys. Res. Letters* 37: doi: 10.1029/2010GL044728.
- Palandri JL, Kharaka YK, 2004, A compilation of rate parameters of water-mineral interaction kinetics for application to geochemical modeling. USGS Open File Report 2004-1068. 64pp.
- Pau GSH, Bell JB, Pruess K, Almgren AS, Lijewski MJ, Zhang K, 2010, High resolution simulation and characterisation of density-driven flow of CO₂ storage in saline aquifers. *Adv. Water Res.* 33: 443-455.
- Plummer LN, Wigley TML, Parkhurst DL, 1978, The kinetics of calcite dissolution in CO₂-water systems at 5° to 60° and 0.0 to 1.0 atm CO₂. *Am. J. Sci.* 278: 179-216.
- Pham VTH, Lu P, Aagaard P, Zhu C, Hellevang H ,2011, On the potential of CO₂-water-rock interactions for CO₂ storage using a modified kinetic model. *Intern. J. Greenhouse Gas Control* 5: 1002-1015.
- Riaz A, Hesse M, Tchelepi HA, Orr FM, 2006, Onset of convection in a gravitationally unstable diffusive boundary layer in porous media. *J. Fluid Mech.* 548: 87-111.
- Rimstidt, J.D. and Barnes, H.L., 1980. The kinetics of silica-water reactions. *Geochim Cosmochim. Acta* 44: 1683-1699.
- Schulz HD, 2006, Quantification of early diagenesis: Dissolved constituents in pore water and signals in the solid phase, In: Marine Geochemistry, HD Schulz and M Zabel (eds.), 2nd edition, Springer Verlag Berlin Heidelberg, 73-124.
- Sibson RH, 1974, Frictional constraints on thrust, wrench and normal faults, *Nature* 249: 542-544.

- Sonnenthal, E., Spycher, N., 2000. Drift-scale coupled processes model: analysis and model report (AMR) N0120/U0110, Yucca Mountain Nuclear Waste Disposal Project. Lawrence Berkeley National Laboratory, Berkeley, CA.
- Steefel, C.I. (2001) GIMRT, version 1.2: Software for modeling multicomponent, multidimensional reactive transport. User's Guide, UCRL-MA-143182. Livermore, California: Lawrence Livermore National Laboratory.
- Vieillard P, 2002, A new method for the prediction of Gibbs Free Energies of formation of phyllosilicates (10 Å and 14 Å) based on the electronegativity scale. *Clays Clay Min.* 50: 352-363.
- Vilarrasa V, Carrera J, Bolster D, Dentz M, 2013, Semianalytical solution for CO₂ plume shape and pressure evolution during CO₂ injection in deep saline formations. *Transp. Porous Med.* 97: 43-65.
- Walton, A.G., 1967. The Formation and Properties of Precipitates. Interscience Publ, New York, 232p.
- White AF, 1995, Chemical weathering rates of silicate minerals in soils. In White AF and Brantley SL (Eds.), Chemical weathering rates of silicate minerals. Mineralogical Society of America, *Rev. Mineralogy* 31: 407-461.
- Xu, T, Spycher N, Sonnenthal EL, Zheng L, Pruess K, 2012, TOUGHREACT User's guide: A simulation program for non-isothermal multiphase reactive geochemical transport in variably saturated geologic media. Lawrence Berkeley National Laboratory Draft Report, Berkeley, California, 241 p.
- Xu T, Chen S, Zhang D, 2006, Convective stability analysis of the long-term storage of carbon dioxide in deep saline aquifers. *Adv. Water Res.* 29: 397-407.
- Zhu C, Veblen DR, Blum AE, Chipera SJ, 2006, Naturally weathered feldspar surfaces in the Navajo Sandstone aquifer, Black Mesa, Arizona: electron microscope characterization. *Geochim. Cosmochim. Acta* 70: 4600-4616.
- Ziabakhsh-Ganji, Z., Kooi, H. (2012) An Equation of State for thermodynamic equilibrium of gas mixtures and brines to allow simulation of the effects of impurities in subsurface CO₂ storage. *Intern.I J. Greenhouse Gas Control*, 11, 21-34.



CONTACT US

Canberra

Dr Richard Aldous
Chief Executive

GPO Box 463, Canberra, ACT 2601
Ph: + 61 2 6120 1600
Fax: + 61 2 6273 7181
Email: raldous@co2crc.com.au

Ms Carole Peacock
Business Manager

GPO Box 463, Canberra, ACT 2601
Ph: + 61 2 6120 1605
Fax: + 61 2 6273 7181
Email: cpeacock@co2crc.com.au

Melbourne

Dr Matthias Raab
Program Manager for CO₂ Storage

School of Earth Science
The University of Melbourne
VIC 3010
Ph: +61 3 8344 4309
Fax: +61 3 8344 7761
Email: mraab@co2crc.com.au

Mr Barry Hooper
Chief Technologist

Room 232/Level 2
School of Electrical & Electronic
Engineering, The University
of Melbourne, VIC 3010
Ph: + 61 3 8344 6622
Fax: + 61 3 9347 7438
Email: bhooper@co2crc.com.au

Mr Rajindar Singh
Otway Project Manager

School of Earth Science
The University of Melbourne
VIC 3010
Ph: + 61 3 8344 9007
Fax: + 61 3 8344 7761
Email: rssingh@co2crc.com.au

Sydney

Prof Dianne Wiley
Program Manager for CO₂ Capture

The University of New South Wales
UNSW Sydney, 2052
Ph: + 61 2 9385 4755
Email: dwiley@co2crc.com.au

Adelaide

Prof John Kaldi
Chief Scientist

Australian School of Petroleum
The University of Adelaide, SA 5005
Ph: + 61 8 8303 4291
Fax: + 61 8 8303 4345
Email: jkaldi@co2crc.com.au

Perth

Mr David Hilditch
Commercial Manager (CO₂TECH)

PO Box 1130, Bentley
Western Australia 6102
Ph: + 61 8 6436 8655
Fax: + 61 8 6436 8555
Email: dhilditch@co2crc.com.au

researching carbon capture and storage

